A proposal to Jefferson Lab PAC26

Semi-Inclusive Spin Asymmetries on the Nucleon Experiment

The " Semi-SANE " Experiment

X. Zheng
Argonne National Laboratory, Argonne, Illinois.

D. Dutta, H. Gao, K. Kramer, W. Xu
Duke University, Durham, North Carolina.

P. Markowitz
Florida International University, Miami, Florida.

K. Baker
Hampton University, Hampton, Virginia.

P. Bosted(Co-Spokesperson), A. Bruell, J.-P. Chen, E. Chudakov, R. Ent, D. Gaskell, D.W. Higinbotham, M. Jones (Co-Spokesperson), A. Saha
Jefferson Lab, Newport News, Virginia.

W. Korsch
University of Kentucky, Lexington, Kentucky.

J.J. Kelly
University of Maryland, College Park, Maryland.

K. Paschke
University of Massachusetts, Amherst, Massachusetts.

V. Punjabi
Norfolk State University, Norfolk, Virginia.

P. Ulmer
Old Dominion University, Norfolk, Virginia.

V. Kubarovsky, P. Stoler
Rensselaer Polytechnic Institute, Troy, New York.

R. Gilman, C. Glashausser, X. Jiang (Co-Spokesperson)[a], G. Kumbartzki, K. McCormick, R. Ransome
Rutgers University, Piscataway, New Jersey.

[a]Contact person, email: jiang@jlab.org

Seonho Choi, Z.-E. Meziani, K. Slifer, P. Solvignon
Temple University, Philadelphia, Pennsylvania.

D. Crabb, D. Day (Co-Spokesperson), N. Liyanage, O.A. Rondon, K. Wang
University of Virginia, Charlottesville, Virginia.

T. Averett, C. Perdrisat, L. Pentchev
College of William and Mary, Williamsburg, Virginia.

A. Agalaryan, R. Asaturyan, H. Mkrtchyan, S. Stepanyan, and V. Tadevosyan
Yerevan Physics Institute, Yerevan, Armenia.

E. Brash, G. Huber, C. Xu
University of Regina, Regina, Canada.

V. I. Kravtsov, Yu. M. Melnik, K. E. Shestermanov, L. F. Soloviev, A. N. Vasiliev
Institute of High Energy Physics, Protvino, Russia.

Abstract: We propose to measure the spin asymmetries in semi-inclusive deep-inelastic $\vec{p}(e,e'h)X$ and $\vec{d}(e,e'h)X$ reactions ($h = \pi^+, \pi^-, K^+$ and K^-) on longitudinally polarized NH_3 and LiD targets. The large acceptance *BETA* detector, in the same configuration as in the approved "SANE" experiment, will be used to detect the scattered electrons. The HMS spectrometer will be used to detect the leading hadrons in coincidence ($z = 0.5 \sim 0.7$). The high statistic data will allow a spin-flavor decomposition in the region of $x = 0.12 \sim 0.41$ at $Q^2 = 1.21 \sim 3.14$ GeV^2. Four leading order methods and two next-to-leading order methods of flavor decomposition will be applied independently to provide consistency cross-checks. Especially, a next-to-leading order spin-flavor decomposition of Δu_v, Δd_v and $\Delta\bar{u} - \Delta\bar{d}$ will be extracted based on the measurement of the combined asymmetries $A_{1N}^{\pi^+-\pi^-}$. The possible flavor asymmetry of the polarized sea will be addressed in this experiment. The precision data from this experiment will significantly improve our knowledge of the flavor structure of the nucleon spin for both valence and sea quarks. The much improved knowledge on the moments of the polarized quark distributions will provide benchmark tests for theoretical models and lattice QCD calculations. In addition to the double-spin asymmetry A_{1N}^h, the target single-spin asymmetry A_{UL}^h will also be measured as by-products. Especially, the term $A_{UL}^{sin2\phi_h}$, which at the leading order is produced only through a non-vanishing T-odd Collins fragmentation function. Within the same data set, the deviation from the naive factorization assumption, which translates into the systematic uncertainties of the leading order flavor decomposition, will be clearly demonstrated by comparing the combined asymmetry $A_{1N}^{\pi^++\pi^-}$ with the inclusive asymmetry A_{1N}. A total of 25 days of new beam time at 6 GeV in Hall C is requested. In addition, permission is requested for parasitic data taking during the 6 GeV longitudinal target runs of the "SANE" experiment (2 days) to test spin-duality in $\vec{p}(\vec{e},e'\pi^+)X$ reaction through the resonance region.

Contents

1 Introduction

The last decade has seen remarkable progress in the knowledge of the polarized quark distributions $\Delta q_f(x)$. The most precise and clearly interpreted experimental tool has been inclusive deep-inelastic lepton scattering (DIS) applied at the CERN and SLAC. However, the information available from inclusive DIS process has inherent limitations. As the cross sections are only sensitive to e_q^2, the square of the quark charge, an inclusive DIS experiment probes quarks and anti-quarks on an equal footing, therefore is not sensitive to the symmetry breaking in the sea sector. From the inclusive data alone, it would only possible to determine combinations of $\Delta q + \Delta \bar{q}$, but never Δq_v and $\Delta \bar{q}$ separately. Only one particular flavor non-singlet combination can be directly inferred through DIS measurements, i.e. $\Delta q_3(x, Q^2) = \Delta u + \Delta \bar{u} - \Delta d - \Delta \bar{d} = 6(g_1^p - g_1^n)$. The additional assumption of $\mathrm{SU}(3)_f$ flavor symmetry allows the hyperon beta decay data to constrain the first moments of Δq. The celebrated result of this approach is that quark helicities seem to make a small net contribution to the nucleon spin, and the strange sea appears to be negatively polarized.

The sensitivity to each individual quark flavor is realized in semi-inclusive deep inelastic scattering (SIDIS) in which one of the leading hadrons is also detected. Since the leading hadrons from the current fragmentation carry information about the struck quark's flavor, detection of the leading hadron effectively "tags" the quark flavor. Therefore, SIDIS offers an unique opportunity for determining the spin, flavor, and sea structure of the nucleon [1], thereby significantly enriching our understanding of QCD and the nucleon structure. High precision polarized SIDIS data on the proton and the neutron allows a flavor decomposition of nucleon spin structure, which could lead to the discovery of a possible flavor-asymmetry in the polarized sea. Recently, the HERMES collaboration published the results of a leading order spin flavor decomposition from polarized proton and deuteron data, and for the first time extracted the $\bar{u}, \bar{d}$ and $s = \bar{s}$ sea quark polarization [2,3]. Unlike the predictions of several theoretical models, HERMES found that within the available statistics $\Delta \bar{u} - \Delta \bar{d}$ is consistent with an unbroken $\mathrm{SU}(2)_f$ symmetry.

At high enough energy transfer the quark-scattering and hadron production processes factorize at the leading order: the cross section becomes a simple product of quark distributions and quark fragmentation functions. At moderate energies, the extent to which leading order factorization applies is an open question which could only be answered with precision experimental data. The HERMES data has demonstrated that, within the experimental precision, the semi-inclusive double-spin asymmetries A_{1N}^h $(N = p, d)$ at $\langle Q^2 \rangle = 2.5$ GeV^2 agree reasonably well with the SMC data [4] which was obtained at $\langle Q^2 \rangle = 10$ GeV^2. Recent Jefferson Lab Hall B results [5] of $A_{1p}^{\pi^+}$ asymmetry, which is at $\langle Q^2 \rangle = 1.8$ GeV^2, are also shown to be consistent with the HERMES and the SMC data. This non-trivial agreement indicates that the expected leading order factorization violation is not large around Q^2 of 2.0 GeV^2, and the semi-inclusive asymmetry A_{1N}^h has a rather weak Q^2 dependence, just like the inclusive asymmetry A_{1N}. The apparent "precocious scaling" suggests that at modest Q^2, information on the quark distributions is reasonably well-preserved in semi-inclusive reactions. Recently, Ji, Ma and Yuan explicitly showed[6] that QCD factorization is valid for SIDIS with hadrons emitted in the current fragmentation region with low transverse momentum $p_{\perp h} \ll Q$. Factorization of spin-dependent cross sections in SIDIS and Drell-Yan has also been shown for low $p_{\perp h}$ case[7].

Jefferson Lab is actively pursuing the opportunity of an energy upgrade to 12 GeV. Semi-inclusive experiments will be a rich program with the upgrade if the leading order factorization can be demonstrated to hold at a reasonable level. With the high luminosity available at Jefferson Lab, it is possible to perform precision measurements at a large scattering angle, which brings Q^2 close to that of HERMES while investigating a similar x region. To quantitatively answer the question of leading order factorization at 6-12 GeV, it is crucial to perform precision measurements on observables that are sensitive to the violation of leading order factorization. Recently, a schematic strategy of leading order factorization tests has been suggested[8] which requires no prior knowledge of fragmentation functions nor parton distributions. The experimental challenge in this strategy is to measure the combined double-spin asymmetry $A_{1N}^{\pi^++\pi^-}$. If leading order factorization holds perfectly, $A_{1N}^{\pi^++\pi^-}$ will turn out to be identical to the inclusive A_{1N} asymmetry due to the exact cancellation of the fragmentation functions. Their difference, $A_{1N}^{\pi^++\pi^-} - A_{1N}$, gives a clear indication on the size of the next-to-leading-order contributions which violate the naive leading order x-z factorization. In practice, the combined asymmetry $A_{1N}^{\pi^++\pi^-}$ poses more experimental challenges, since knowledge of phase spaces and detector's efficiencies are required. Preliminary results from HERMES demonstrated perfect agreements between $A_{1N}^{\pi^++\pi^-}$ and A_{1N} for both proton and deuteron, indicating that the NLO correction terms are not large at $\langle Q^2 \rangle = 2.5$ GeV^2.

This experiment is specifically designed to have well controlled phase spaces and hadron detection efficiencies such that the combined asymmetries $A_{1N}^{\pi^+\pm\pi^-}$, in addition to the individual asymmetries A_{1N}^h ($h = \pi^+, \pi^-, K^+, K^-$), can be determined with high precision to give a better lever-arm in the flavor decomposition. At Q^2 of $1.21 \sim 3.14$ GeV^2, a leading order spin-flavor decomposition of the nucleon spin structure will be performed in the region of $x = 0.12 \sim 0.41$. The much improved statistics over the HERMES data will present us with the first opportunity to probe the possible flavor asymmetry of the light sea quark polarization. At the high-x bins, this experiment overlaps with the recent Hall A experiment[9] (E99117) which extracted ratios of $\Delta u/u$ and $\Delta d/d$ from the inclusive asymmetry A_{1n} at high-x. The consistency check between semi-inclusive data from this experiment and the inclusive data of E99117 provides the validity test of the various flavor decomposition methods in semi-inclusive experiments.

It was recently pointed out by Christova and Leader[8] that if the combined asymmetries $A_{1N}^{\pi^+-\pi^-}$ are measured with a high enough precision, quark polarization Δu_v, Δd_v and $\Delta\bar{u} - \Delta\bar{d}$ can be extracted at leading order without the complication of fragmentation functions. Even at the next-to-leading order, information on the valence quark polarizations is well preserved in the combined asymmetries $A_{1N}^{\pi^+-\pi^-}$ since the gluon-quark and quark-gluon splitting terms are canceled in the $\pi^+ - \pi^-$ observables due to isospin symmetry and charge conjugation invariance [8].

In addition to a direct extraction of $\Delta\bar{u} - \Delta\bar{d}$, one can also chose to access the polarized sea asymmetry through precise measurements of Δu_v and Δd_v in the valence region. The key point here [10] is that the the Bjorken sum rule establishes the link between the first moments of the sea-quark and the valence-quark polarizations at all orders of QCD. Written in terms of the moment $\Delta_1 q = \int_0^1 dx\Delta q$, Bjorken sum rule reads

$$
\begin{aligned}
\Delta q_3 \equiv a_3 &= \left[\Delta_1 u(Q^2) + \Delta_1 \bar{u}(Q^2)\right] - \left[\Delta_1 d(Q^2) + \Delta_1 \bar{d}(Q^2)\right] \\
&= \left|\frac{g_A}{g_v}\right| = 1.2670 \pm 0.0035 \quad \textit{in all QCD orders.}
\end{aligned} \tag{1}
$$

therefore,

$$
\Delta_1\bar{u} - \Delta_1\bar{d} = \frac{1}{2}\left|\frac{g_A}{g_v}\right| - \frac{1}{2}(\Delta_1 u_v - \Delta_1 d_v) \quad \textit{in all QCD orders.} \tag{2}
$$

Using Eq. 2, and the earlier SIDIS results of HERMES $\Delta_1 u_v$ and $\Delta_1 d_v$, it was speculated [10] that the spin-flavor asymmetry could be as large as: $\Delta_1\bar{u} - \Delta_1\bar{d} = 0.235 \pm 0.097$. Considering that the NMC data [12] gives $\int_0^1(\bar{d} - \bar{u})dx = 0.147 \pm 0.039$, this estimate ends up close to the Pauli-blocking model prediction [13] of $(\Delta\bar{u} - \Delta\bar{d})/(\bar{d} - \bar{u}) = 5/3$.

2 Physics Motivation

The principle goal of spin-dependent SIDIS experiments is to perform flavor decomposition of nucleon spin structure taking advantage of flavor tagging. In this section, we first express the SIDIS cross sections and asymmetries at leading order (LO) and the next-to-leading order (NLO) before summarizing the HERMES results of the leading order "purity method". We will outline two new methods of flavor decomposition for this experiment: the Christova-Leader method at leading order and the next-to-leading order, and the leading order "fixed-z purity" method. We will also address the issue of leading order factorization and methods of "effectively measuring" the next-to-leading order contribution following the strategy of Christova and Leader [8]. Theoretical models of polarized light sea asymmetry is summarized to motivate our measurement of $\Delta\bar{u} - \Delta\bar{d}$. Existing experimental evidence suggesting the leading order factorization at the relevant Q^2 are summarized at the end of this section. The next-to-leading order predictions of various experimental observables of this experiment are presented in detail in Appendix–A. The detail of leading order "fixed-z" purity formalism is presented in Appendix–B. Throughout this proposal, SU(2) isospin symmetry and charge conjugation invariance are assumed and heavy quark contributions are neglected. In addition, we assume a symmetrical strange quark distribution and polarization ($s(x) = \bar{s}(x)$, $\Delta s(x) = \Delta\bar{s}(x)$).

2.1 SIDIS cross sections at leading order and the next-to-leading order

At the leading order of α_s, the SIDIS process is factorized into a hard quark scattering followed by a quark hadronization process, as shown in the first diagram of Fig. 1. The "naive factorization " assumption, on which the SMC and HERMES analysis were based, implies that the spin-independent (σ^h) and the spin-dependent ($\Delta\sigma^h$) hadron-h production cross sections factorize into the x-dependent quark distributions and the z-dependent quark fragmentation functions:

$$\sigma^h(x,z) = \sum_i e_f^2 q_f(x) \cdot D_{q_f}^h(z), \quad \Delta\sigma^h(x,z) = \sum_i e_f^2 \Delta q_f(x) \cdot D_{q_f}^h(z), \tag{3}$$

where $x = Q^2/2M\nu$, $z = E_h/\nu$, e_f is quark charge, $q_f(x)$ and $\Delta q_f(x)$ are quark distributions and polarization of flavor f ($f = u, d, \bar{u}, \bar{d}, s, \bar{s}$). The functions $D_{q_f}^h(z)$ represent the probability that a quark f fragments into a hadron h.

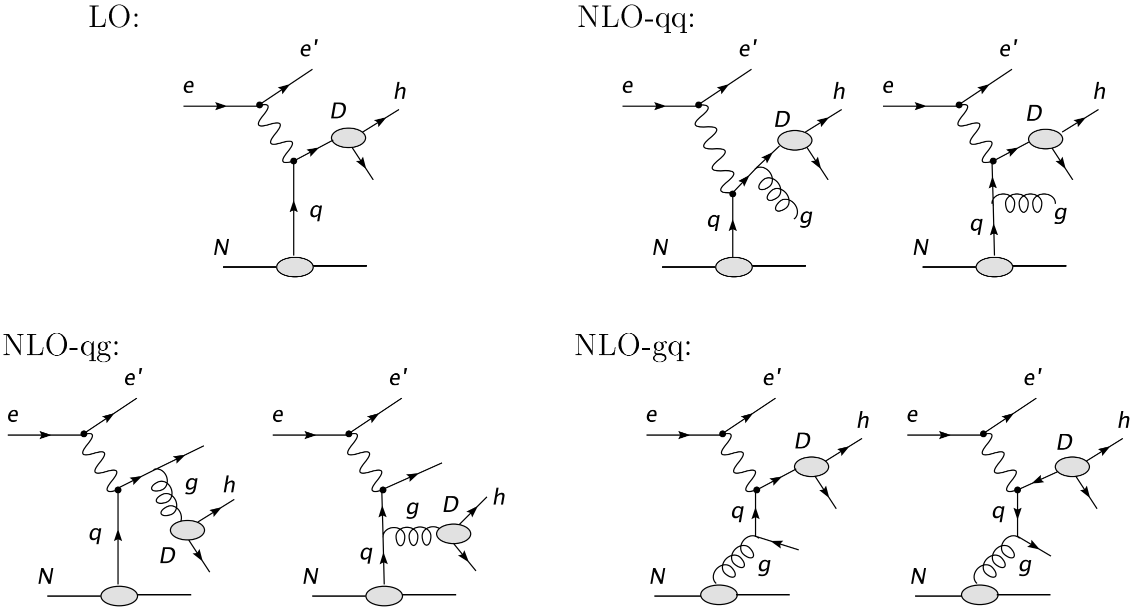

Figure 1: Semi-inclusive deep inelastic scattering diagrams at leading order (LO) and the next-to-leading order (NLO).

The naive $x-z$ factorization is violated at the next-to-leading order when the one-gluon diagrams in Fig. 1 are considered. However, the exact form of this violation has been well-known [14]. At NLO, the terms of $q(x) \cdot D(z)$ and $\Delta q(x) \cdot D(z)$ in Eq. 3 are added with the double convolutions of the type $q \otimes \mathcal{C} \otimes D$ and $\Delta q \otimes \Delta C \otimes D$ in which $\mathcal{C}$ and ΔC are well-known Wilson coefficients [15]:

$$[q \otimes C \otimes D](x,z) = \int_x^1 \frac{dx'}{x'} \int_z^1 \frac{dz'}{z'} q\left(\frac{x}{x'}\right) C(x',z') D\left(\frac{z}{z'}\right). \tag{4}$$

Not only are x and z mixed through the double convolutions at the next-to-leading order, the unpolarized cross section σ^h also depends on the virtual photon variable $y = (E_0 - E')/E_0$ due to the longitudinal component of the virtual photon.

We define the short-hand notation:

$$qD + \frac{\alpha_s}{2\pi} q \otimes C \otimes D = q \left[1 + \otimes \frac{\alpha_s}{2\pi} C \otimes \right] D, \tag{5}$$

at NLO instead of Eq. 3, we have:

$$\begin{aligned}
\sigma^h(x,z) &= \sum_f e_f^2 q_f \left[1 + \otimes \frac{\alpha_s}{2\pi} \mathcal{C}_{qq} \otimes \right] D^h_{q_f} \\
&+ \left(\sum_f e_f^2 q_f\right) \otimes \frac{\alpha_s}{2\pi} \mathcal{C}_{qg} \otimes D^h_G + G \otimes \frac{\alpha_s}{2\pi} \mathcal{C}_{gq} \otimes \left(\sum_f e_f^2 D^h_{q_f}\right), \qquad (6) \\
\Delta\sigma^h(x,z) &= \sum_f e_f^2 \Delta q_f \left[1 + \otimes \frac{\alpha_s}{2\pi} \Delta C_{qq} \otimes \right] D^h_{q_f} \\
&+ \left(\sum_f e_f^2 \Delta q_f\right) \otimes \frac{\alpha_s}{2\pi} \Delta C_{qg} \otimes D^h_G + \Delta G \otimes \frac{\alpha_s}{2\pi} \Delta C_{gq} \otimes \left(\sum_f e_f^2 D^h_{q_f}\right). \qquad (7)
\end{aligned}$$

For any given form of the parton distributions, the SIDIS cross sections can be calculated numerically [16] according to Eq. 6 and Eq. 7. It is also well-known that in Mellin-n space, the double-convolutions factorize into simple products under moments, and the parton distributions can be recovered by an inverse Mellin transformation with all moments of Wilson coefficients already calculated [17].

2.2 Double-spin asymmetries at leading order and the next-to-leading order

Considering the beam and target polarization (P_B and P_T), and the dilution factor ($f^h = \sigma^h_{pol.N}/\sigma^h_{allN}$), which reflects the presence of unpolarized nucleons in the target, the experimental double-spin asymmetry [3] for a longitudinally polarized beam on a longitudinally polarized target is [b] :

$$A^h_{\parallel} = f^h P_B P_T \cdot \mathcal{P}_{kin} \cdot A^h_{1N}, \tag{8}$$

the kinematic factor $\mathcal{P}_{kin}$ is:

$$\mathcal{P}_{kin} = \mathcal{D} \cdot (1 + \gamma\eta) \cdot \frac{1+R}{1+\gamma^2}, \tag{9}$$

in which

$$\begin{aligned}
\eta &= \frac{2\gamma(1-y)}{2-y}, \qquad \mathcal{D} = \frac{1-(1-y)\epsilon}{1+\epsilon\cdot R}, \\
\epsilon^{-1} &= 1 + 2(1+\nu^2/Q^2)\tan^2(\theta_e/2), \qquad (10)
\end{aligned}$$

[b] For the deuteron case, an additional correction of $(1+\frac{3}{2}\omega_D)^{-1}$ with $\omega_D = 0.05 \pm 0.01$ is required to account for the D state in deuteron [18].

$\mathcal{D}$ is the virtual photon polarization, $R(x, Q^2) = \sigma_L/\sigma_T$ accounts for the longitudinal component of the virtual photon and $y = \nu/E_0$, $\gamma^2(x, Q^2) = 4M^2x^2/Q^2$. In the current fragmentation regime, the virtual photon asymmetry A_{1N}^h is defined as:

$$A_{1N}^h(x, Q^2, z) \equiv \frac{\Delta\sigma^h(x, Q^2, z)}{\sigma^h(x, Q^2, z)}. \tag{11}$$

At the leading order, the cross sections in Eq. 11 take the form of Eq. 3. At the next-to-leading order, the cross sections are replaced by Eq. 6 and Eq. 7. The next-to-leading order and leading order predictions [16,19] of the pion asymmetries are plotted in Fig. 2, as functions of z for the bin of $x = 0.203$ of this experiment. In principle, the asymmetry A_{1N}^h depends on both variables x and z, its x-dependency comes from the parton distributions and z-dependency comes from the fragmentation functions. Accurate knowledge of the fragmentation functions is crucial in order to extract quark polarizations from the measured asymmetries. However, in some special combinations, if σ^h and $\Delta\sigma^h$ happen to have similar z-dependencies, as their ratio, the asymmetry will end up with a weak or even vanishing z-dependency. This type of cancellation can provide us with much cleaner observables to access quark polarizations without the complication of fragmentation functions. For example, Christova and Leader pointed out [8] that at the leading order, under the assumptions of SU(2) isospin symmetry and charge conjugation invariance, the fragmentation functions canceled exactly in the combined $h^+ \pm h^-$ double-spin asymmetries. Furthermore, if strange quark contribution can be neglected, the semi-inclusive asymmetry $A_{1N}^{\pi^+ + \pi^-}$ is reduced to the inclusive asymmetry A_{1N}. Even at the next-to-leading order, the z-dependence of $A_{1N}^{\pi^+ \pm \pi^-}$ is predicted to be very small [19], as shown in the lower panels of Fig. 2. Another example is the deuteron asymmetry $A_{1d}^{\pi}(x, z)$ which is predicted to have a very weak z-dependence at both leading order and the next-to-leading order. In the $p + n$ system, the SU(2) isospin symmetry guarantees an exact cancellation between the z-dependencies of $\Delta\sigma^h$ and σ^h for u and d quarks, leaving only the relative z-dependencies of $\bar{u}$ and $\bar{d}$ quarks to generate the overall z-dependency for $A_{1d}^{\pi}(x, z)$. As a result, $A_{1d}^{\pi}(x, z)$ is practically z-independent, and one has $A_{1d}^{\pi^+}(x, z) = A_{1d}^{\pi^-}(x, z) = A_{1d}$ at $x > 0.1$, as shown in Fig. 2 and Fig. 28 of Appendix–A.

2.3 The HERMES leading order purity method and results

Both the SMC and the HERMES analysis explicitly assumed the $x - z$ factorization of Eq. 3 at the leading order, the asymmetries are related to the parton polarizations through linear relations as:

$$A_{1N}^h(x, Q^2, z) = \frac{\sum_f e_f^2 \Delta q_f(x, Q^2) \cdot D_f^h(z, Q^2)}{\sum_f e_f^2 q_f(x, Q^2) \cdot D_f^h(z, Q^2)}. \tag{12}$$

The HERMES analysis used the "purity method" to achieve leading order flavor decomposition [20]. In Eq. 12, a "purity matrix" $\mathcal{P}_f^h(x, Q^2, z)$ was defined such that:

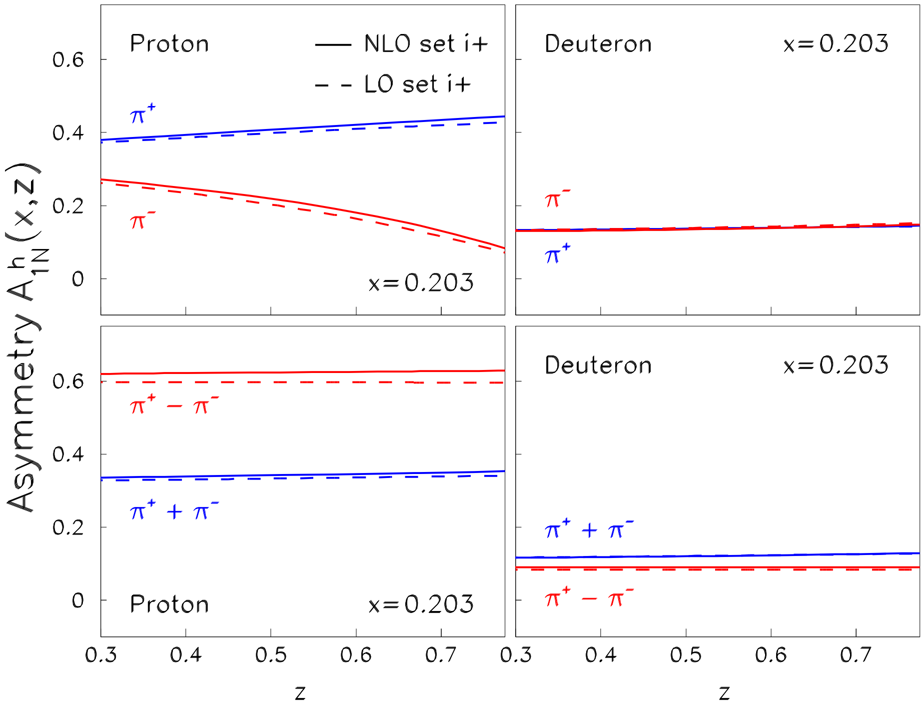

Figure 2: The next-to-leading-order (solid lines) and the leading order (dashed lines) pion asymmetry predictions [19] using de Florian and Sassot's parton distributions [16] set $i+$ are plotted for $\langle Q^2 \rangle = 2.2$ GeV^2 and $x = 0.203$ as functions of z.

$$A_{1N}^h(x, Q^2, z) \equiv \sum_f \mathcal{P}_f^h(x, Q^2, z) \cdot \frac{\Delta q_f(x, Q^2)}{q_f(x, Q^2)}, \tag{13}$$

where

$$\mathcal{P}_f^h(x) = \frac{e_f^2 q_f(x) \int dz D_f^h(z)}{\sum_i e_i^2 q_i(x) \int dz D_i^h(z)}, \tag{14}$$

and the explicit Q^2 notation has been omitted for simplicity. The "purity method" integrates over all experimental allowed z-range such that SIDIS events are included as much as possible to improve statistical accuracy. The exact values of $\mathcal{P}_f^h(x, Q^2, z)$ in the HERMES analysis were obtained through a detailed Monte Carlo simulation which was based on the Lund fragmentation model [21] and taking into account of the experimental phase space and detector efficiencies. The parameters used in the fragmentation model were fine-tuned in order to reproduce the measured hadron yields.

Integrating over hadrons with $0.2 < z < 0.8$, HERMES extracted five flavor quark polarizations:

$$\vec{Q} = \left(x\Delta u, x\Delta d, x\Delta\bar{u}, x\Delta\bar{d}, x\Delta s\right), \tag{15}$$

from a data base of measured double-spin asymmetries

$$\vec{A} = \left(A_{1p}^{\pi^+}, A_{1p}^{\pi^-}, A_{1d}^{\pi^+}, A_{1d}^{\pi^-}, A_{1d}^{K^+}, A_{1d}^{K^-}, A_{1p}, A_{1d}\right) \tag{16}$$

by solving the relations of $\vec{A} = \mathcal{P}_f^h(x) \cdot \vec{Q}$. The recent HERMES data of deuteron asymmetries [2] are shown in Fig. 3 in comparison with the SMC data [4].

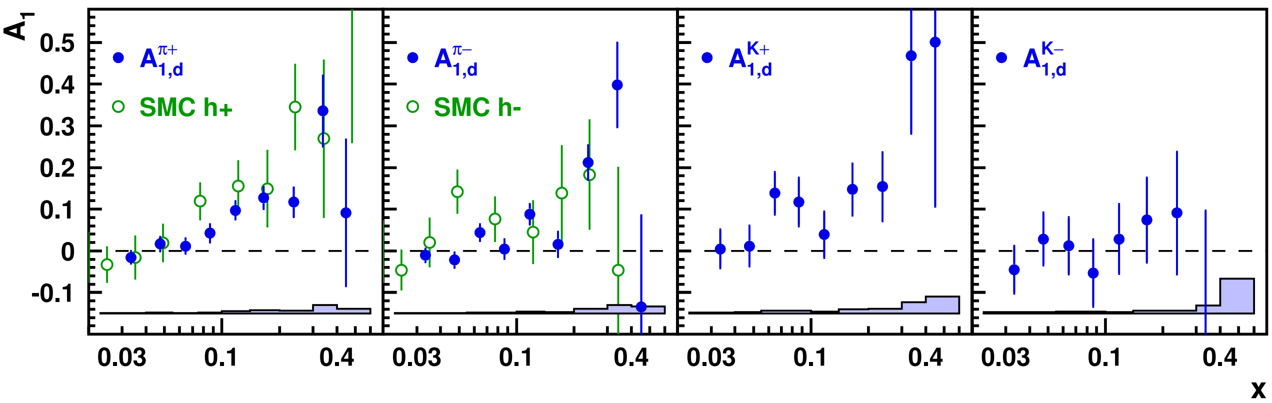

Figure 3: The semi-inclusive deuteron asymmetry A_{1d}^h form HERMES [2] and SMC [4].

The HERMES results of flavor decomposition are shown in Fig 4. As expected, u-quarks are strongly polarized in the direction of proton spin, while d-quarks are polarized opposite to the proton spin. The u and d sea quarks carry a small amount of spin while the s-quark polarization is consistent with zero. Fig. 4 also shows the HERMES results of $x(\Delta\bar{u} - \Delta\bar{d})$ together with the prediction of a broken $SU(2)_f$

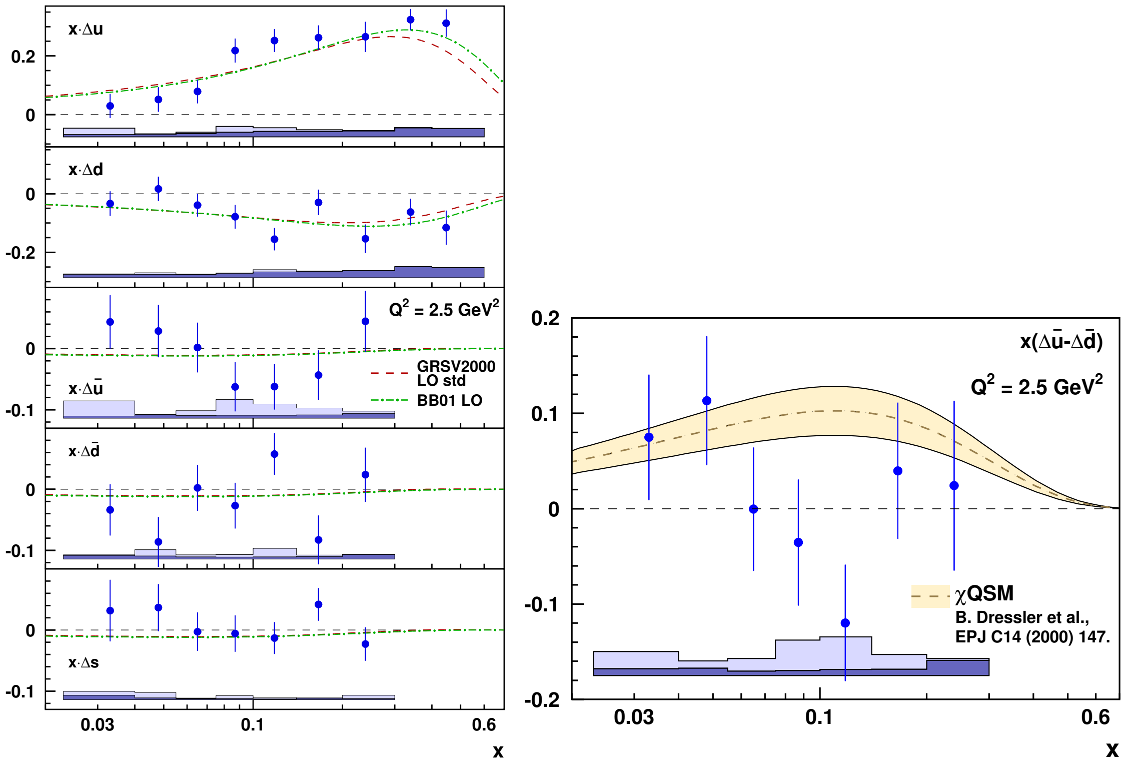

Figure 4: The left panel shows the HERMES results [2] of the polarized quark distributions at a common scale of $Q^2 = 2.5$ GeV^2 for u, $\bar{u}$, d, $\bar{d}$, and $s+\bar{s}$ quark flavors versus x in comparison with two different parameterizations [22,23]. The right panel shows the difference of the polarized light sea $x(\Delta\bar{u} - \Delta\bar{d})$ as a function of x. The error bars are statistical, while the shaded bands at the bottom indicate the systematic uncertainties.

symmetry [24,25]. The data are consistent with an unbroken $\mathrm{SU}(2)_f$ symmetry in the polarized light sea.

The HERMES results left a lot of room to be improved, at least with respect to the statistics, especially on $\Delta\bar{u}-\Delta\bar{d}$. In addition, the validity and the stability of the leading order purity method needs to be independently verified. As pointed out by many authors, the issue of leading order factorization violation, the size of the next-to-leading order contributions and the intrinsic uncertainties of the fragmentation Monte Carlo simulation need to be quantitatively addressed[8] at the level appropriate to the sea contribution.

2.4 Spin-flavor decomposition at leading order and the next-to-leading order

This experiment will use four independent leading order and two independent next-to-leading order methods to achieve spin-flavor decomposition. At leading order, the result from the LO Christova-Leader method will be cross checked against the LO global fit method, the "fixed-z purity" method and the Monte Carlo purity method. At the next-to-leading order, the result of NLO Christova-Leader method will be cross checked with the NLO global fit method. Within the same data set, the naive x-z leading order factorization assumption can be tested quantitatively by comparing the combined asymmetry $A_{1N}^{\pi^++\pi^-}$ with the well known inclusive asymmetry A_{1N}. Their differences will clearly demonstrate the size of the leading order factorization violation due to the next-to-leading order contributions. In this section, we will give a brief outline of these flavor decomposition methods. The formalism details are provided in Appendix–B.

The Christova-Leader method at LO and NLO

At the leading order, under SU(2) isospin symmetry and charge conjugation invariance, the fragmentation functions canceled exactly in the combined asymmetry $A_{1N}^{\pi^+\pm\pi^-}$. In the quantities related to $\sigma^{\pi^+}-\sigma^{\pi^-}$, the strange-quark does not contribute. From Appendix–B, we have :

$$
\begin{aligned}
A_{1p}^{\pi^+-\pi^-} &= \frac{\Delta\sigma_p^{\pi^+}-\Delta\sigma_p^{\pi^-}}{\sigma_p^{\pi^+}-\sigma_p^{\pi^-}} = \frac{4\Delta u_v-\Delta d_v}{4u_v-d_v}, \\
A_{1d}^{\pi^+-\pi^-} &= \frac{\Delta\sigma_d^{\pi^+}-\Delta\sigma_d^{\pi^-}}{\sigma_d^{\pi^+}-\sigma_d^{\pi^-}} = \frac{\Delta u_v+\Delta d_v}{u_v+d_v}.
\end{aligned} \tag{17}
$$

Therefore:

$$
\begin{aligned}
(\Delta u_v)_{LO} &= \frac{1}{5}\left[\left(4u_v-d_v\right)\cdot A_{1p}^{\pi^+-\pi^-}+(u_v+d_v)\cdot A_{1d}^{\pi^+-\pi^-}\right)\right], \\
(\Delta d_v)_{LO} &= \frac{1}{5}\left[4\left(u_v+d_v\right)\cdot A_{1d}^{\pi^+-\pi^-}-(4u_v-d_v)\cdot A_{1p}^{\pi^+-\pi^-}\right)\right], \\
(\Delta u_v-\Delta d_v)_{LO} &= \frac{1}{5}\left[2\left(4u_v-d_v\right)\cdot A_{1p}^{\pi^+-\pi^-}-3(u_v+d_v)\cdot A_{1d}^{\pi^+-\pi^-}\right)\right].
\end{aligned} \tag{18}
$$

From the inclusive DIS data, we have:

$$g_1^p(x,Q^2) - g_1^n(x,Q^2) = \frac{1}{6}\Delta q_3(x,Q^2)|_{LO}, \tag{19}$$

the non-singlet Δq_3 is defined as:

$$\Delta q_3(x,Q^2) \equiv (\Delta u + \Delta\bar{u}) - (\Delta d + \Delta\bar{d}). \tag{20}$$

The polarized light sea asymmetry can be extracted through:

$$(\Delta\bar{u} - \Delta\bar{d})|_{LO} = 3(g_1^p - g_1^n)|_{LO} - \frac{1}{2}(\Delta u_v - \Delta d_v)|_{LO}. \tag{21}$$

A similar relation holds at the next-to-leading order.

At the next-to-leading order, under SU(2) isospin symmetry and charge conjugation invariance, the NLO convolution terms become much simpler in quantities that related to $\sigma^{\pi^+} - \sigma^{\pi^-}$. Since the gq and qg terms in Eq. 6 and Eq. 7 are identical for π^+ and π^- production, they drop out in the combined asymmetry [8]:

$$\begin{aligned} A_{1p}^{\pi^+-\pi^-} &= \frac{(4\Delta u_v - \Delta d_v)\left[1 + \otimes(\alpha_s/2\pi)\Delta C_{qq}\otimes\right](D^+ - D^-)}{(4u_v - d_v)\left[1 + \otimes(\alpha_s/2\pi)\mathcal{C}_{qq}\otimes\right](D^+ - D^-)}, \\ A_{1d}^{\pi^+-\pi^-} &= \frac{(\Delta u_v + \Delta d_v)\left[1 + \otimes(\alpha_s/2\pi)\Delta C_{qq}\otimes\right](D^+ - D^-)}{(u_v + d_v)\left[1 + \otimes(\alpha_s/2\pi)\mathcal{C}_{qq}\otimes\right](D^+ - D^-)}. \end{aligned} \tag{22}$$

in which Δu_v and Δd_v evolve as non-singlets and do not mix with other densities. Therefore, measurements of $A_{1N}^{\pi^+-\pi^-}$ on proton and deuteron can determine Δu_v and Δd_v at the next-to-leading order without any consideration of gluon and sea distributions. The double-convolution terms in Eq. 22 are expected to introduce negligible z-dependency in $A_{1N}^{\pi^+-\pi^-}$ at the kinematics of this experiment, as demonstrated in the calculation of de Florian and Sassot [19] in Fig. 2 and Fig. 28. The solution of Eq. 22 needs to follow an iterative procedure and the order from higher-x to lower-x, since the measured Δq_v values at higher-x feed into the solution of lower-x through the convolution terms. Initial assumptions of Δq_v high-x can be taken from a theoretical ansatz that respects the positivity limit.

The first moment of $\Delta u_v - \Delta d_v$ is linked with the moment of $\Delta\bar{u} - \Delta\bar{d}$ through the Bjorken sum rule at all QCD orders [11]. The Bjorken sum rule, written in terms of the moment $\Delta_1 q = \int_0^1 dx\Delta q$,

$$\begin{aligned} \Delta_1 q_3 &\equiv \left[\Delta_1 u(Q^2) + \Delta_1\bar{u}(Q^2)\right] - \left[\Delta_1 d(Q^2) + \Delta_1\bar{d}(Q^2)\right] \\ &= \left|\frac{g_A}{g_v}\right| = 1.2670 \pm 0.0035 \quad \textit{valid in all QCD orders.} \end{aligned} \tag{23}$$

Therefore, valid in all QCD orders, we have:

$$\Delta_1\bar{u} - \Delta_1\bar{d} = \frac{1}{2}\left|\frac{g_A}{g_v}\right| - \frac{1}{2}(\Delta_1 u_v - \Delta_1 d_v). \tag{24}$$

Furthermore, a well-defined procedure has been given [11] to obtain the moment $\Delta_1 u_v - \Delta_1 d_v$ directly from the measured asymmetries $A_{1p}^{\pi^+-\pi^-}$ and $A_{1d}^{\pi^+-\pi^-}$ without first solving Eq. 22 point-to-point. The stability of this procedure has been demonstrated [11] using the HERMES-1999 data.

Global fits at leading order and the next-to-leading order

The formalism of SIDIS asymmetry including the next-to-leading order contributions has been well established. Several global fitting efforts have been carried out in recent years when SIDIS asymmetry data became available. The NLO global fitting procedures of SIDIS data follows the similar strategy as in the NLO inclusive DIS fitting, except that one includes both inclusive and semi-inclusive data in the fitting process with different weighting. The combinations of $\Delta q + \Delta\bar{q}$ have been well constrained through the inclusive g_1^p and g_1^n data alone, the added SIDIS data sets are used only to provide separation between Δq and $\Delta\bar{q}$. Once the SIDIS asymmetry data, A_{1N}^h, becomes available, similar global fitting procedure will be carried out by our theory collaborators [19].

The leading-order "fixed-z purity" method

The HERMES leading-order "purity" method can be much simplified if high statistics data are available at a well-defined z-value for all asymmetries. Instead of obtaining the "purity matrix" over a large z range as integrated quantities in a Monte Carlo, a well-localized "fixed-z purity" can be defined as described in detail in Appendix–B. The measured asymmetries are related with quark polarization through linear relations, for example:

$$A_{1p}^{\pi^+}(x,z) = \frac{4\Delta u + \Delta\bar{d} + (4\Delta\bar{u} + \Delta d)\,\lambda_\pi + 2\Delta s\xi_\pi}{4u + \bar{d} + (4\bar{u} + d)\,\lambda_\pi + 2s\;\xi_\pi}, \quad etc. \tag{25}$$

where $\lambda_\pi(z) = D_\pi^-(z)/D_\pi^+(z)$ and $\xi_\pi(z) = D_s^\pi(z)/D_\pi^+(z)$ are ratios of fragmentation functions. These ratios are better known than the fragmentation function themselves. The existing parameterizations [26] obtained from e^+e^- data provide reasonable accuracies to start with. Data from HERMES had shown [27] that $\lambda_\pi(z) = D_\pi^-/D_\pi^+$ closely follows $(1-z)/(1+z)$, as predicted by Field and Feynman [28].

For a given x-bin, at a fixed z-value, each asymmetry measurement provides an independent constraint on a linear combination of quark polarizations. In addition to the semi-inclusive asymmetries A_{1N}^h, the well-known inclusive asymmetry A_{1p} and A_{1d} impose extra constraints on $\Delta u + \Delta\bar{u}$, $\Delta d + \Delta\bar{d}$ and $\Delta s + \Delta\bar{s} = 2\Delta s$. In this experiment, we will extract 5 quark polarizations:

$$\vec{Q} = \left(x\Delta u, x\Delta d, x\Delta\bar{u}, x\Delta\bar{d}, x\Delta s\right), \tag{26}$$

from measurements of 10 double-spin asymmetries

$$\vec{A} = \left(A_{1p}^{\pi^+}, A_{1p}^{\pi^-}, A_{1d}^{\pi^+}, A_{1d}^{\pi^-}, A_{1p}^{K^+}, A_{1p}^{K^-}, A_{1d}^{K^+}, A_{1d}^{K^-}, A_{1p}, A_{1d}\right) \tag{27}$$

by solving the over-constrained set of equations $\vec{A} = \mathcal{P}_f^h(x)\cdot\vec{Q}$. The determination of these coefficients requires inputs from unpolarized quark distributions and ratios of fragmentation functions, the exact knowledge of the fragmentation function becomes irrelevant.

Spin observables to test the leading order factorization

If we further assume $\Delta s = \Delta\bar{s} \approx 0$ in the valence region, the fragmentation functions are canceled at the leading order in the combined asymmetry $A_{1N}^{\pi^+ + \pi^-}$, as discussed in detail in Appendix–B, such that:

$$A_{1p}^{\pi^+ + \pi^-}(x, Q^2, z) = \frac{\Delta\sigma_p^{\pi^+} + \Delta\sigma_p^{\pi^-}}{\sigma_p^{\pi^+} + \sigma_p^{\pi^-}} = \frac{4(\Delta u + \Delta\bar{u}) + \Delta d + \Delta\bar{d}}{4(u + \bar{u}) + d + \bar{d}} \equiv A_{1p}(x, Q^2),$$
$$A_{1d}^{\pi^+ + \pi^-}(x, Q^2, z) = \frac{\Delta\sigma_d^{\pi^+} + \Delta\sigma_d^{\pi^-}}{\sigma_d^{\pi^+} + \sigma_d^{\pi^-}} = \frac{\Delta u + \Delta d + \Delta\bar{u} + \Delta\bar{d}}{u + d + \bar{u} + \bar{d}} \equiv A_{1d}(x, Q^2). \quad (28)$$

The combined asymmetry $A_{1N}^{\pi^+ + \pi^-}$ reduces to the inclusive asymmetry A_{1N} under the leading order x-z factorization assumption. The relation $A_{1N}^{\pi^+ + \pi^-}(x, Q^2, z) = A_1(x, Q^2)$ is a rather strong condition to satisfy, since the left-hand side involves the hadron observable z while the right-hand side doesn't. The deviation of $A_{1N}^{\pi^+ + \pi^-}$ from the inclusive A_{1N} asymmetry "effectively" measures the relative importance of the contribution from the next-to-leading order terms.

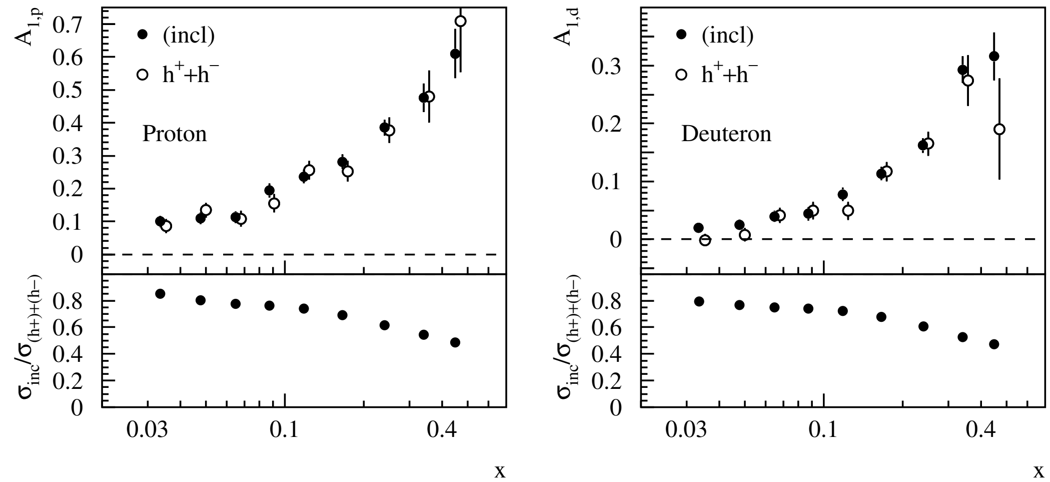

Figure 5: The HERMES inclusive asymmetries on the proton and the deuteron are compared with the respective semi−inclusive combined $h^+ + h^-$ asymmetries. The top panels show the asymmetries, where the hadron tagged asymmetry is offset in x for presentation. The lower panel shows the ratio of the uncertainties, $\sigma(A_1)/\sigma(A_{1N}^{h^+ + h^-})$.

The HERMES experiment extracted the combined asymmetry $A_{1N}^{h+\bar{h}}$ as shown in Fig. 5 in comparison with the inclusive asymmetry A_{1N}. The near perfect agreement of $A_{1N}^{h+\bar{h}}$ with A_{1N} at $\langle Q^2 \rangle = 2.5$ GeV^2 indicated that the next-to-leading order correction terms are small or mostly canceled in the asymmetries and the target fragmentation contribution has a negligible impact to the asymmetries. Should similar agreements be observed at Jefferson Lab energy, with $\langle Q^2 \rangle = 2.2$ GeV^2 for this experiment, parton polarizations can be reliably extracted through the leading order interpretation of SIDIS asymmetries.

2.5 $\Delta\bar{u} - \Delta\bar{d}$: the flavor asymmetry in the polarized sea

A few years ago, Fermilab experiment E866 reported measurements of the yield ratio of Drell-Yan muon pairs from an 800 GeV/c proton beam incident on hydrogen and deuterium [29,30]. The data suggested a significantly asymmetric light-quark sea distribution over an appreciable range in x; the asymmetry and $\bar{d}/\bar{u}$ peaked around $x = 0.18$, as shown in Fig. 6. Furthermore, based on the E866 data and the CTEQ4M global-fit values of $\bar{u} + \bar{d}$, the values of $\bar{d}(x) - \bar{u}(x)$ were extracted, and it was concluded that: $\int_0^1 \left[\bar{d}(x) - \bar{u}(x)\right] dx = 0.118 \pm 0.012$. Many theoretical models, including meson cloud model, chiral-quark model, Pauli-blocking model, instanton model, chiral-quark soliton model and statistical model, have been proposed to explain the $\bar{d}/\bar{u}$ asymmetry. These models can describe the $\bar{d} - \bar{u}$ reasonably well. However, they all have difficulties explaining the $\bar{d}/\bar{u}$ data at $x > 0.2$.

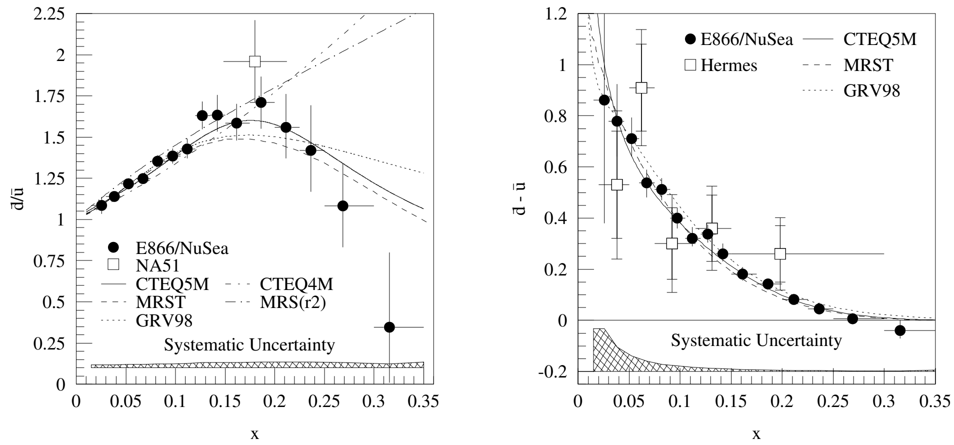

Figure 6: The Fermilab E866 results [29,30]. The left plot shows the ratio $\bar{d}/\bar{u}$ as a function of x, the right plot shows the extracted value of $\bar{d}(x) - \bar{u}(x)$ together with the HERMES semi-inclusive DIS results.

Since the unpolarized sea demonstrates a significant flavor asymmetry, one naively speculates a sizable flavor asymmetry exists for the polarized sea in the same x-region . Indeed, many of the theoretical models have specific implications for the spin structure of the nucleon sea, for example, the Pauli-blocking model and the instanton model both predict a large $\Delta\bar{u}$, $\Delta\bar{d}$ asymmetry, with $\Delta\bar{u} > \Delta\bar{d}$, namely, $\int_0^1 [\Delta\bar{u}(x) - \Delta\bar{d}(x)]dx = \frac{5}{3} \cdot \int_0^1 [\bar{d}(x) - \bar{u}(x)]dx \approx 0.2$. In the chiral-quark soliton model, $\Delta\bar{u} - \Delta\bar{d}$ appears in leading-order (N_c^2) in a $1/N_c$ expansion, while the unpolarized distribution $\bar{d} - \bar{u}$ appears in the next-to-leading order (N_c). On the other hand, those meson cloud models which only include π-meson predict $\Delta\bar{u} = \Delta\bar{d} = 0$ since they reside in spin-0 π-meson. By considering a vector meson (ρ) cloud, non-zero sea quark polarization were predicted. A summary of theoretical predictions [31] of $I_\Delta = \int_0^1 [\Delta\bar{u}(x) - \Delta\bar{d}(x)]dx$ are given in Table. 1. If the flavor asymmetry of the polarized sea is indeed as large as the predictions of many model shown in Table. 1, it would imply that a significant fraction of the Bjorken sum, $\int_0^1 [g_1^p(x) - g_1^n(x)]dx$, comes from the flavor asymmetry of the polarized nucleon sea.

Model	I_Δ prediction	Authors and References
Meson cloud (π-meson)	0	Eichten *et al.* [32], Thomas [33]
Meson cloud (ρ-meson)	$\simeq -0.007$ to -0.027	Fries *et al.* [34]
Meson cloud ($\pi - \rho$ interference)	$= -6 \int_0^1 g_1^p(x)dx \simeq -0.7$	Boreskov *et al.* [35]
Meson cloud (ρ and $\pi - \rho$ interference)	$\simeq -0.004$ to -0.033	Cao *et al.* [36]
Meson cloud (ρ-meson)	< 0	Kumano *et al.* [37]
Meson cloud ($\pi - \sigma$ interference)	$\simeq 0.12$	Fries *et al.* [38]
Pauli-blocking (bag model)	$\simeq 0.09$	Cao *et al.* [36]
Pauli-blocking (ansatz)	$\simeq 0.3$	Gluck *et al.* [39]
Pauli-blocking	$= \frac{5}{3} \int_0^1 [\bar{d}(x) - \bar{u}(x)]dx \simeq 0.2$	Steffens [13]
Chiral-quark soliton	0.31	Dressler [40]
Chiral-quark soliton	$\simeq \int_0^1 2x^0.12[\bar{d}(x) - \bar{u}(x)]dx$	Wakamatsu *et al.* [41]
Instanton	$= \frac{5}{3} \int_0^1 [\bar{d}(x) - \bar{u}(x)]dx \simeq 0.2$	Dorokhov [42]
Statistical	$\simeq \int_0^1 [\bar{d}(x) - \bar{u}(x)]dx \simeq 0.12$	Bourrely *et al.* [43]
Statistical	$> \int_0^1 [\bar{d}(x) - \bar{u}(x)]dx \simeq 0.12$	Bhalerao [44]

Table 1: A summary [31] of theoretical predictions of $I_\Delta = \int_0^1 [\Delta\bar{u}(x) - \Delta\bar{d}(x)]dx$.

2.6 The target single-spin asymmetry A_{UL}

As by-products, this experiment will also produce high statistic data on the target single-spin asymmetry A_{UL}. Especially interesting is the $\sin 2\phi$ moment of A_{UL}, as shown in Eq. 29, is caused only by a non-vanishing chiral-odd Collins fragmentation function $H_1^{\perp q}$. CLAS eg1b data has shown a noticeable $A_{UL}^{\sin 2\phi}$, as plotted in Fig. 7 together with the theory prediction [45] of Efremov *et al.*. A confirmation of such a non-zero single-spin asymmetry is certainly very important. We expect to improve

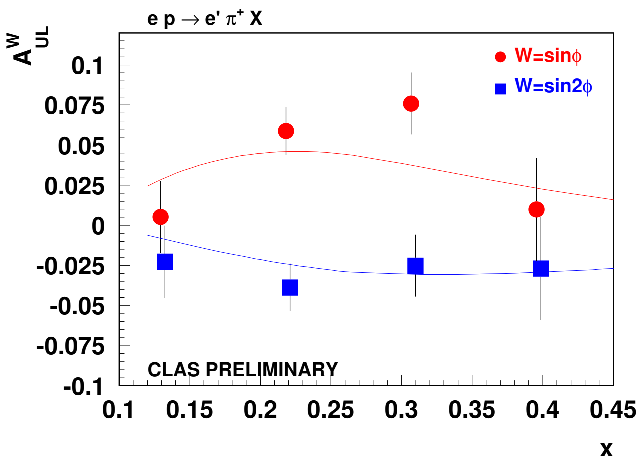

Figure 7: Azimuthal moment of target single-spin asymmetry $A_{UL}^{\sin\phi}$ and $A_{UL}^{\sin 2\phi}$ from CLAS EG1b $\vec{p}(e,e'\pi^+)X$ data [5]. The kinematic cuts are $0.5 < z < 0.8$ and $W' > 1.1$ GeV. Curves are from A. Efremov *et al.* [45]

the statistical accuracy on $A_{UL}^{\sin 2\phi}$ by a factor of three over the existing CLAS data.

$$A_{UL}^{\sin 2\phi} = S_L \cdot \sin 2\phi \sum_q e_q^2 x h_{1L}^{\perp q}(x) \cdot H_1^{\perp q}(z), \tag{29}$$

2.7 *Existing data suggests leading order factorization*

The quark-hadron duality argument of Close and Isgur [46] suggested that leading order factorization might work at the Jefferson Lab energy. Existing cross section data also supports such leading order x-z factorization at JLab energy. In the left panel of Fig. 8, preliminary $p(e,e'\pi^-)X$ cross section from the Hall C E00-108 experiment is compared with a SIDIS Monte Carlo. The simulation, which is based on the leading order factorization assumption, reproduces the cross section data almost perfectly. The lack of any clear resonance structure at $z < 0.7$ ($W' > 1.5$ GeV) indicates that the contributions from exclusive resonance production channels are not large in the cross section when W' is above the Δ mass, confirming the observation of a Cornell experiment [47] at $E_0 = 11$ GeV. In the right panel of Fig. 8, CLAS 5.7 GeV data in the $p(e,e'\pi^+)X$ reaction is shown to have a common z-dependence for different x-bins, confirming the observation of x-z factorization in an earlier Cornell experiment [48] at 11 GeV.

The existing asymmetry data also suggests leading order x-z factorization at 6 GeV. In the left panel of Fig. 9, clear agreement of $A_{1p}^{\pi^+}$ between HERMES and CLAS (eg1b run) data are shown. In addition, the semi-inclusive asymmetries clearly agree with the inclusive asymmetry A_{1p}, indicating the strong domination of current-quark fragmentation in the semi-inclusive data. The CLAS data corresponding to $\langle Q^2\rangle = 1.77$ GeV^2 and a rather low missing mass cut of $W' > 1.1$ GeV. Furthermore, the CLAS $A_{1p}^{\pi^+}$ data demonstrated no z-dependency, as shown in the right panel of

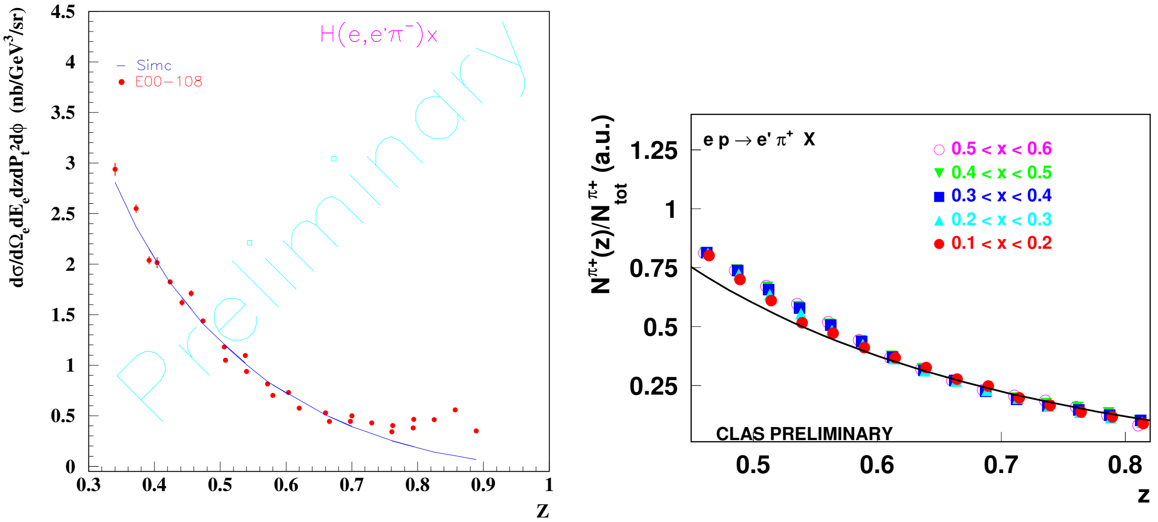

Figure 8: In the left panel, the absolute cross sections (red dots) from E00-108 in the $p(e, e'\pi^-)X$ channel at $x = 0.3$ are shown to agree with a SIDIS Monte Carlo simulation (solid line). In the right panel, CLAS 5.7 GeV data in the $p(e, e'\pi^+)X$ channel is shown to have a common z-dependence for different x-bins.

Fig. 9. Similar z-independent behavior of $A_{1p}^{\pi^+}$ and A_{1d}^{h} was also observed in the HERMES data [3] within the statistical uncertainties.

3 The Proposed Measurement

3.1 Overview

We plan to study the $\vec{p}(\vec{e}, e'h)X$ and $\vec{d}(\vec{e}, e'h)X$ reactions ($h = \pi^+, \pi^-, K^+$ and K^-) with longitudinally polarized NH_3 and LiD targets in Hall C with a 6 GeV polarized electron beam. Relative yields will be determined for different combinations of beam and target spin orientations and the combined asymmetries $A_{1N}^{\pi^+ \pm \pi^-}$ will be constructed in addition to the various double-spin asymmetries A_{1N}^{h}. As shown in Fig. 10, the HMS spectrometer will be located at 10.8° beam right as the hadron arm detector. The HMS will be set at a central momentum of 2.71 GeV/c and either positive or negative polarity. The standard HMS aerogel and gas Cherenkov detectors will be used for particle identification of kaons and pions. For the electron arm, we will use a combination of large calorimeter (*BigCal*), lucite array and gas Cherenkov. This is the same detector package that will be used in the approved experiment [51] E03-109,“ Spin Asymmetries on the Nucleon Experiment” (SANE) that was designated as the Big Electron Telescope Array (*BETA*). *BETA* will be centered at 30° beam left. A detailed description of *BETA* is given in the SANE proposal. Since this is a coincidence experiment, and the HMS can be used for target position reconstruction, from coincidence timing and HMS vertex cuts one can eliminate the majority of the background in *BETA*.

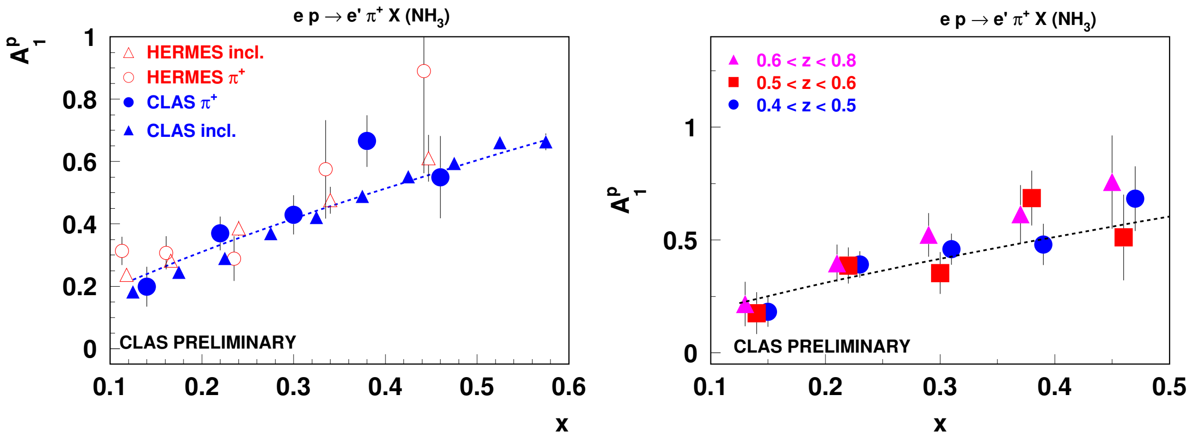

Figure 9: Left panel: CLAS $A_{1p}^{\pi^+}$ data compared with HERMES data, the inclusive A_1 asymmetry of CLAS and HERMES are also plotted for comparison. Right panel: the CLAS asymmetry $A_{1p}^{\pi^+}$ are plotted for different z-bins.

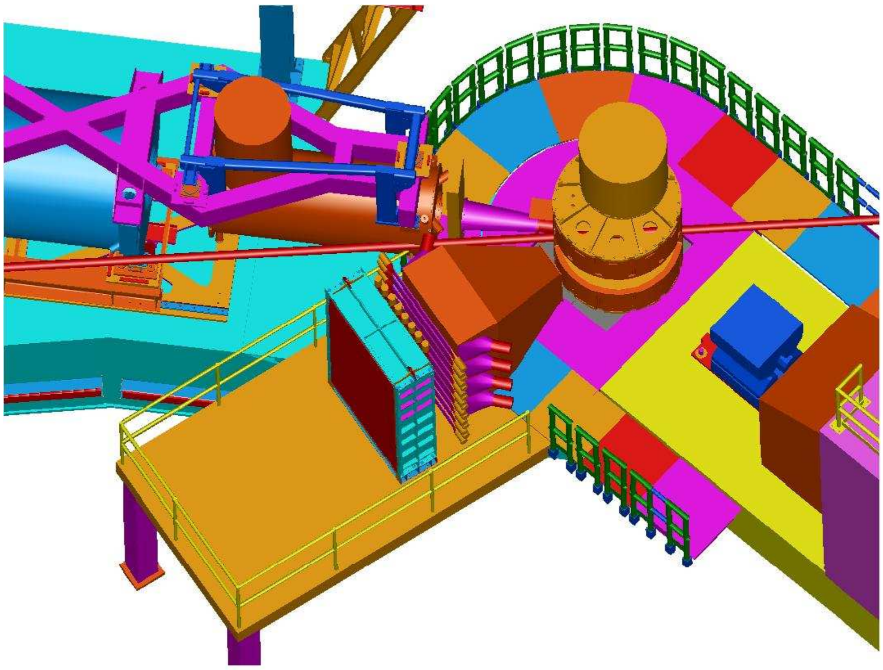

Figure 10: A top view of the floor arrangement. The thick red line represents the beam which is incident from the right (the beam dump is to the left of the picture). The electron-arm detector (*BETA*) , with *BigCal* in the back, the gas Cherenkov in the front and the lucite array in between, is at 30° beam left. The HMS spectrometer is shown at 10.8° beam right. The SOS spectrometer is on beam left at a backward angle.

3.2 Kinematics and phase space

The definitions of the kinematics variables are the following: Bjorken-x, which indicates the fractional momentum carried by the struck quark, $x = Q^2/(2\nu M_N)$, M_N is the nucleon mass. The momentum of the outgoing hadron is p_h and the fraction of the virtual photon energy carried by the hadron is: $z = E_h/\nu$. W is the invariant mass of the whole hadronic system and W' is the invariant mass of the hadronic system without the detected pion. We have:

$$\begin{aligned} W^2 &= M_N^2 + Q^2(\frac{1}{x} - 1), \\ W'^2 &= (M_N + \nu - E_\pi)^2 - |\vec{q} - \vec{p}_\pi|^2. \end{aligned} \tag{30}$$

We have chosen to cover the highest possible W with a 6 GeV beam, $2.31 < W < 3.09$ GeV, corresponds to $0.12 < x < 0.41$ and $1.21 < Q^2 < 3.14$ (GeV/c)^2. We have also chosen to detect the leading fragmentation hadron which carries $z > 0.5$ of the energy transfer to favor the current fragmentation. The value of W' is also chosen to be as high as possible (1.50$\sim$2.20 GeV) to avoid contributions from the resonance structures. The central kinematic values for each x-bins are listed in Table 2.

In the two-dimensional plot [49] of z vs η_{CM}, where the center-of-mass rapidity $\eta_{CM} = \frac{1}{2} ln \frac{E+P_L^\star}{E-P_L^\star}$ is defined in the center-of-mass frame, as shown in Fig. 11 for $W = 2.5$ GeV, the rapidity gap between the two fragmentation regimes is $\Delta\eta_{CM} = 3.8$ when $z > 0.5$ is required. This condition is well above the regularly used Berger's Criterion of $\Delta\eta_{CM} = 2.0$ for separation of current and target fragmentation [50].

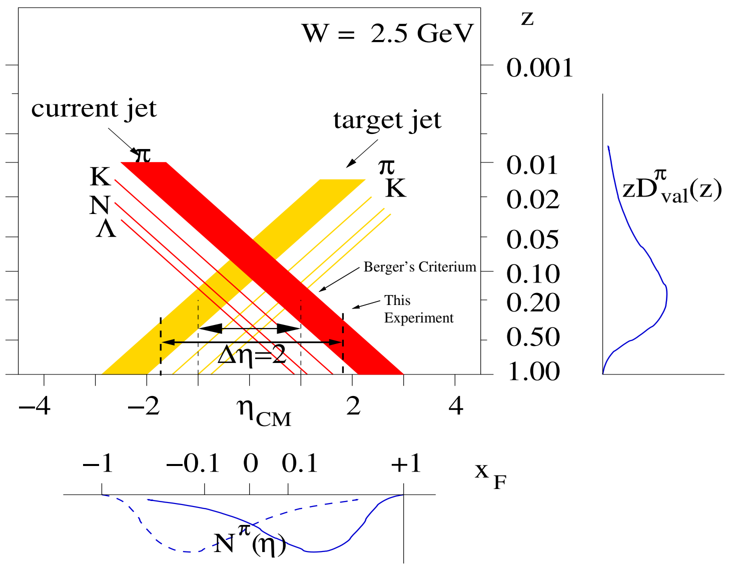

Figure 11: The center-of-mass rapidity gap for $W = 2.5$ GeV, above $z = 0.50$ the current and target fragmentation regime is separated by $\Delta\eta_{CM} = 3.8$. A typical fragmentation function is shown on the side panel with $z = E_\pi/\nu$ and $x_F = p_L^{\pi\star}/|\vec{q}|$.

E′ GeV	θ_e deg.	$\langle x \rangle$	W GeV	Q^2 GeV^2	θ_q deg.	z_π range $(e,e'\pi)$	W'_π GeV	z_K range $(e,e'K)$	W'_K GeV
						p_{HMS} = 2.71 GeV/c, θ_{HMS} = 10.8°			
0.75	30	0.122	3.09	1.21	4.0	0.47-0.57	2.20	0.47-0.58	2.13
1.15	30	0.203	2.85	1.85	6.6	0.50-0.62	1.99	0.51-0.62	1.93
1.55	30	0.298	2.60	2.49	9.4	0.55-0.67	1.76	0.56-0.68	1.70
1.95	30	0.413	2.31	3.14	12.7	0.60-0.74	1.50	0.61-0.75	(1.43)

Table 2: The nominal kinematics for the central calorimeter angle of 30° and the HMS angle of 10.8°. The HMS momentum setting (p_{HMS} = 2.71 GeV/c) and the corresponding z-coverage, W' values are listed. The small shifts in z and W' values for $(e, e'\pi)$ and $(e, e'K)$ reactions reflect the mass difference of kaon and pion. Data of all x-bins will be collected simultaneously. Higher x-bins are not listed in the table.

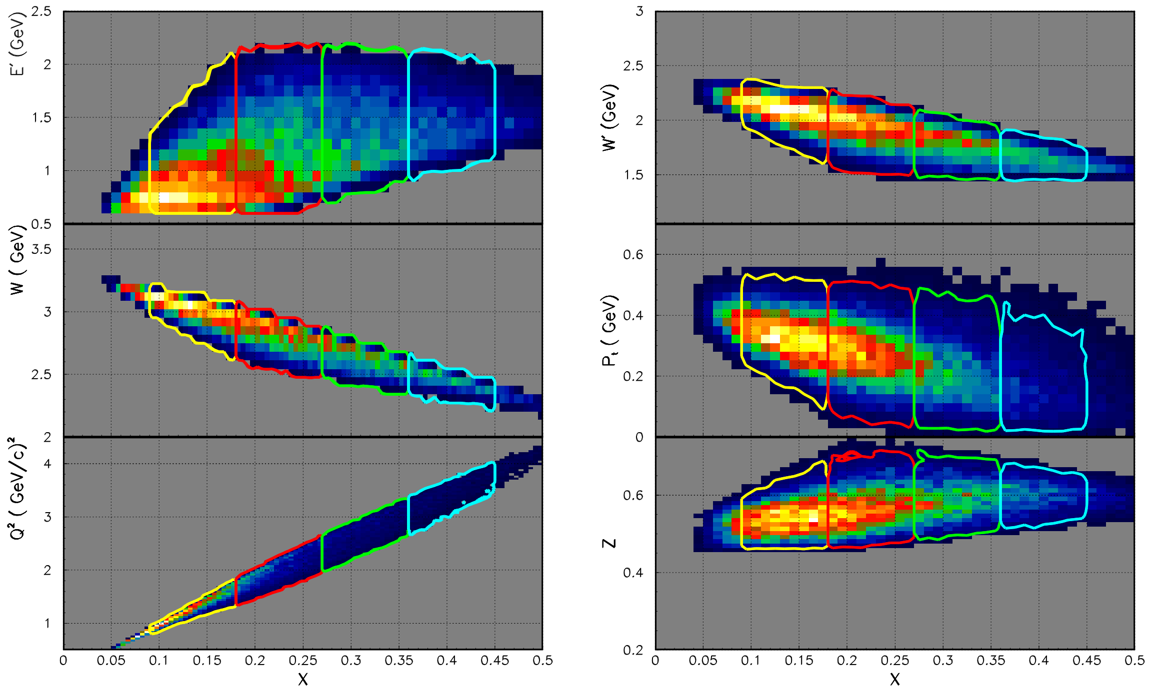

Figure 12: Left panel: the phase space coverage in (Q^2, x) and (W, x) planes with each x-bin in different color. Phase space beyond E' = 2.1 GeV is not plotted. Right panel: phase space coverage in (W', x), (p_t, x) and (z, x) planes. The actual kinematic coverage is wider compared with the nominal values listed in Table 2.

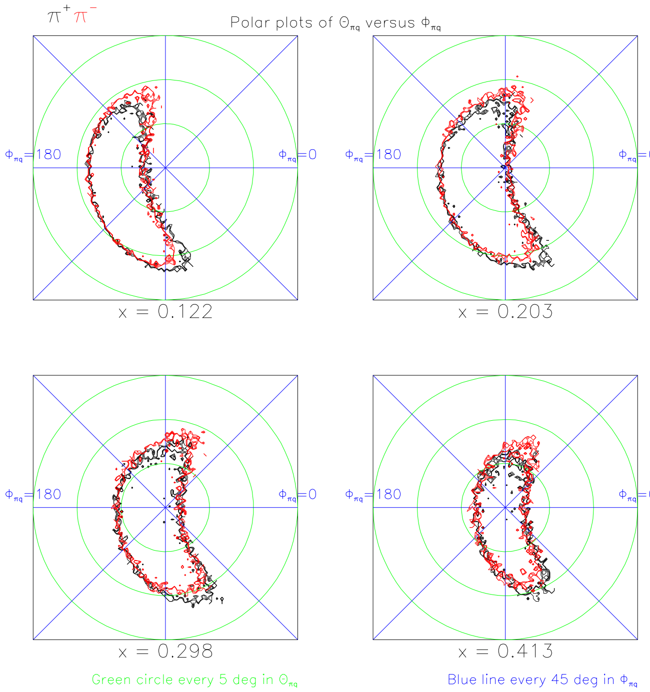

Figure 13: The hadron azimuthal angle ($\phi_{\pi q}$) and polar angle ($\theta_{\pi q}$) coverage for each x-bin. The $\vec{q}$ vector goes into the page at the middle of each plot.

The phase space coverage is obtained from a detailed Monte Carlo simulation which includes realistic spectrometer models, detector geometry as well as the target holding field. The phase space covered in this experiment are shown in Fig. 12. The HMS has a solid angle of 6 msr and a momentum bite of $\pm 10\%$. The *BETA* detector has a solid angle of 210 msr and we only plotted the phase space corresponding to $E' < 2.15$ GeV. The hadron azimuthal angle ($\phi_{\pi q}$) and polar angle ($\theta_{\pi q}$) coverage relative to the direction of $\vec{q}$ is plotted in Fig. 13.

3.3 The experimental observables

The beam and target double-spin asymmetries can be obtained directly from the number of events (N^+ and N^-) observed corresponding to each beam helicity, corrected by the luminosity ratio $\mathcal{L}^+/\mathcal{L}^-$:

$$A_{1N}^h = \frac{1}{f^h P_B P_T \mathcal{P}_{kin}} \cdot \frac{N^+ - N^- \cdot \frac{\mathcal{L}^+}{\mathcal{L}^-}}{N^+ + N^- \cdot \frac{\mathcal{L}^+}{\mathcal{L}^-}} \tag{31}$$

The dilution factors f^h will be measured by comparing the polarized target spectrum with that of the Carbon target, as has been done in earlier experiments at

SLAC, Hall C and Hall B. The typical values of the dilution factors for the NH_3 target are estimated to be $f^{\pi^+} = 0.19 \sim 0.23$, $f^{\pi^-} = 0.16 \sim 0.17$. This estimation has been confirmed in the π^+ case in the CLAS eg1b data, as shown in Fig. 14. Dilution factors for the LiD target are $0.42 \sim 0.45$. Dilution factors for the $(e, e'K)$ measurements are similar to that of the $(e, e'\pi)$ case. The dilution factors are expected to be determined to $\delta f/f \leq 2\%$. The size of the raw asymmetries, $A_{\|}^h$, is expected to be $\leq 7\%$, therefore, we expect $A_{\|}^h \cdot \delta f/f \ll \delta A_{\|}^h$. The statistical uncertainties on the double-spin asymmetry δA_{1N}^h is dominated by $\delta A_{\|}^h$ and is not influenced significantly by the uncertainties of the dilution factor.

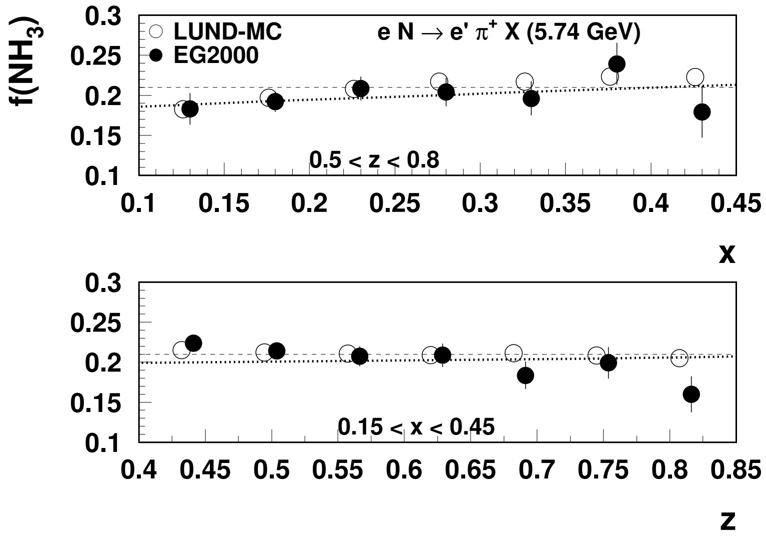

Figure 14: The measured dilution factor of the CLAS π^+ production on a NH_3 target compared with a LUND fragmentation model based Monte Carlo simulation.

The combined beam-target double-spin asymmetry $A_{1N}^{h\pm\bar{h}}$ needs the cross section ratio $\sigma_N^{\bar{h}}/\sigma_N^h$ as an extra input:

$$A_{1N}^{h\pm\bar{h}} = \frac{\Delta\sigma_N^h \pm \Delta\sigma_N^{\bar{h}}}{\sigma_N^h \pm \sigma_N^{\bar{h}}} = \frac{A_{1N}^h \pm A_{1N}^{\bar{h}} \cdot r}{1 \pm r}, \tag{32}$$

where $r = \sigma_N^{\bar{h}}/\sigma_N^h$. In this experiment, $r = \sigma^{\pi^-}/\sigma^{\pi^+} = 0.27 \sim 0.53$ for proton ($0.42 \sim 0.64$ for deuteron). The error propagation follows:

$$(\delta A_{1N}^{h\pm\bar{h}})^2 = \frac{1}{(1 \pm r)^2}\left[(\delta A_{1N}^h)^2 + r^2(\delta A_{1N}^{\bar{h}})^2 + (A_{1N}^{\bar{h}})^2(\delta r)^2 + (A_{1N}^{h\pm\bar{h}})^2(\delta r)^2\right]. \tag{33}$$

Since it does not suffer from the dilution factors, the value of r can be easily determined statistically to $|\delta r|/r \leq 2.0\%$ in this experiment. The systematic uncertainty should also be below 2.0%, since only count ratios over similar phase spaces are involved. In addition, the uncertainty of r is always modulated by the asymmetries, thus, the first two terms in Eq. 33 dominate.

The target single-spin asymmetry A_{UL} will be obtained from the number of events ($N^{\rightarrow}$ and $N^{\leftarrow}$) observed for the target polarization along or against the beam direction, corrected by the luminosity difference $\mathcal{L}^{\rightarrow}/\mathcal{L}^{\leftarrow}$. The luminosity will be monitored by the spectrometer's singles rate. The beam helicity is summed over.

$$A_{UL}^{h} = \frac{1}{fP_B\mathcal{P}_{kin}^{UL}} \cdot \frac{N^{\rightarrow} - N^{\leftarrow} \cdot \dfrac{\mathcal{L}^{\rightarrow}}{\mathcal{L}^{\leftarrow}}}{N^{\rightarrow} + N^{\leftarrow} \cdot \dfrac{\mathcal{L}^{\rightarrow}}{\mathcal{L}^{\leftarrow}}} \tag{34}$$

3.4 The electron detector: BETA

The electron-arm detector consist of a large lead glass calorimeter array, *BigCal*, currently under construction by the Hall C G_{Ep} collaboration, to measure the energy of the electrons. *BigCal* will first be used in experiments 01-109 and 04-013. For SANE, *BigCal* will be augmented with two new detectors to become the Big Electron Telescope Array, *BETA*. The detector closest to the target will be a new segmented threshold gas Cherenkov detector for additional π/e separation. A pion rejection factor of 1000:1 is expected by the combination of BigCal and the gas Cherenkov. In between *BigCal* and the gas Cerenkov is an array of Lucite bars which are used for reconstruction of tracks back to the target, which is important for a single arm experiment like *SANE*. Since this is a coincidence experiment, target reconstruction and cuts will be done using the HMS spectrometer.

The calorimeter array, *BigCal*, combines lead-glass blocks used in the Hall A Real Compton experiment with lead-glass from the Protvino group that was used at Fermilab. Each RCS lead-glass block has a 4x4 cm cross-section and length of 40 cm, while the Protvino lead-glass block has 3.8x3.8 cm cross-section with a length of 45 cm. The lead-glass is being stacked 218 cm in height x 120 cm in width, forming a solid angle of 210 msr at a distance of 3.5 meter from the target. The blocks are individual wrapped with a thin layer of 1 mil thick aluminized mylar so that they are optically isolated from each other. The electron energy resolution is expected to be $5\%/\sqrt{E(\mathrm{GeV})}$. A horizontal and vertical position can be determined by the energy-weighted centroid of the cluster of blocks which share the energy and is expected to be better than 0.5 cm. For coincidence events, the target position will be determined by the HMS to about 0.5 cm so that expected angular resolution for the scattered electron is about 3 mrad. We propose to use the technique of π° mass reconstruction as a means of calibration. This technique has been used in other experiments, such as the RadPhi experiment (E94-016) at JLab and E852 at Brookhaven which employed a large calorimeter. The gain monitoring system will be designed and constructed by the University of Virginia group based on the gain monitoring system that they successfully implemented for the RadPhi experiment.

The gas Cherenkov detector is critical for the rejection of pions while at the same time maintaining a high efficiency for electron detection. Temple University is designing and constructing the gas Cherenkov for SANE. The gas Cherenkov will have a length of 175 cm with the radiator gas occupying a length of 125 cm and the mirrors having a length of 50 cm. A total of eight mirrors will be employed in two columns of 4 and each will have a size of 50 x 70 cm. The mirrors will be designed for point-to-point focusing from the target cell to the photomultiplier tube. The gas Cherenkov will use dry N_2 gas which at 20° C has an index of refraction of 1.000279. This corresponds to a pion momentum threshold of 5.9 GeV/c. The expected number of photo-electrons is 17∼20. The possible contamination of δ-ray knock-out in the Cherenkov are eliminated in a coincidence experiment when a high momentum hadron is required in HMS.

An estimation of the expected resolution for kinematic variables was done using a Monte Carlo simulation. In Table 3, the resolutions, σ, are listed for each x bin. In Fig. 13, the coverage in $\theta_{\pi q}$ and $\phi_{\pi q}$ is shown on a polar plot. The expected range in $\theta_{\pi q}$ is from 0 to 10° and the expect resolution better than a degree at all x. At $x = 0.122$, the $\phi_{\pi q}$ coverage is from 135° to 270°. By $x = 0.413$, the HMS spectrometer is centered along the $\vec{q}$ and $\phi_{\pi q}$ coverage is the full 360° at small $\theta_{\pi q}$ with and emphasis at $\phi_{\pi q} = 90$ and 270°, because the HMS collimator is rectangular. The resolution in $\phi_{\pi q}$ increases with increasing x, since the coverage in $\theta_{\pi q}$ is reduced.

Variable	$\delta\theta_{\pi q}$	$\delta\phi_{\pi q}$	δp_t	δz
$\langle x \rangle = .122$ bin	0.25°	2.4°	0.010	0.006
$\langle x \rangle = .203$ bin	0.28°	3.2°	0.010	0.007
$\langle x \rangle = .298$ bin	0.28°	4.2°	0.010	0.008
$\langle x \rangle = .413$ bin	0.29°	5.9°	0.011	0.008

Table 3: Resolutions (one standard deviation) in each x bin for the kinematic variables $\theta_{\pi q}$, $\phi_{\pi q}$, p_t (GeV/c) and z obtained from the Monte Carlo simulation.

3.5 The hadron detector: HMS

The experiment needs to cleanly identify electrons, pions, and kaons. The plan is to do π/e separation with the lead glass calorimeter in the HMS. The HMS lead glass calorimeter is well suited to identifying electrons by the total energy deposited in the calorimeter. The gas Cherenkov will be used to identify the pions. An aerogel Cherenkov will be used to identify kaons.

In Fig. 15, the index of refraction, n, at which a particle would produce Cherenkov light is plotted as a function of the particle's momentum. The solid black line is for pions and one can see that $n = 1.00215$ is needed to identify pions cleanly. The HMS gas Cherenkov uses C_4F_{10} and is designed to operate at a variety of pressures from 3 atm down to sub-atmospheric pressure. To obtain pion identification above momentum of 2.3 GeV/c , the gas Cherenkov will be operated at 1.5 atm which gives $n = 1.00215$.

The red line in Fig. 15 indicates the threshold for kaon detection by Cherenkov light. The present HMS aerogel detector , which has an aerogel with n = 1.030, will

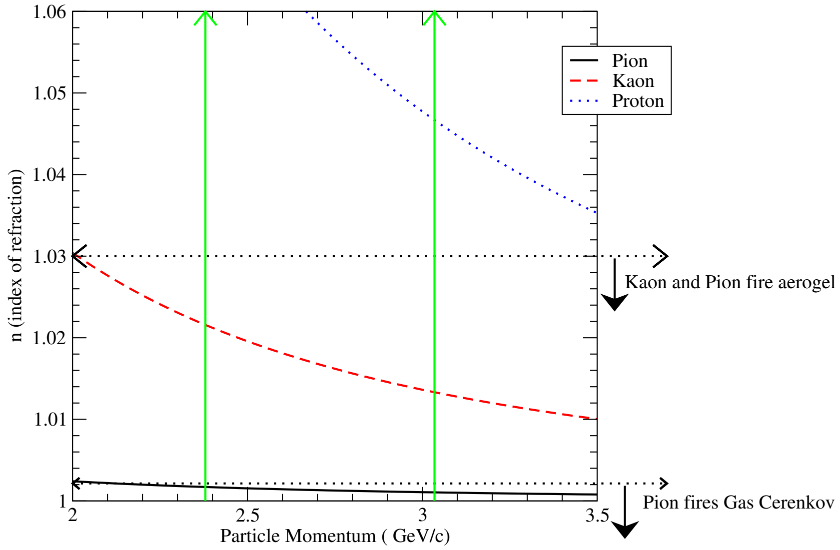

Figure 15: The index of refraction, n, at which Cherenkov light will be produce for a particle versus the particle's momentum.

fire for both kaons and pions. Kaons will be identified as particles which fire the aerogel Cherenkov and not the gas Cherenkov detector. Pions will be identified by firing both the aerogel Cherenkov and the gas Cherenkov detectors and separated from electrons by the energy deposited in the lead glass calorimeter.

3.6 Trigger, time-of-flight resolution and background rates

The hadron trigger in the HMS will be the standard coincidence of 3 out of 4 scintillator planes. The electron arm trigger will be the coincidence of the gas Cherenkov and the calorimeter. The hardware threshold for the Cherenkov trigger will be 0.5 to 1 photoelectrons. For the calorimeter, the analog signals from the individual blocks will be summed in groups of eight to produced a summed signal plus the individual analog signals are passed through to an ADC. The summed analog signal will be sent to a discriminator and a threshold equivalent to 500 MeV energy deposition in the calorimeter will be set. This logical signal will be sent to a TDC. In addition, it will be used as part of a coincidence circuit for the electron arm trigger and eventually for the coincidence between the hadron and electron arms. The Rutgers University group is currently building the electronic modules that will be used in the BigCal for the Hall C G_{Ep} experiment. The BigCal calorimeter is also expected to be used in several other experiments.

To calculate singles rates in the electron arm, a Monte Carlo simulation which includes the target field, the geometry of the target and the magnet's coils was developed by Dr. G. Warren. Rates for electrons, positrons, charge pions, protons and neutrons were calculated. Different codes were incorporated into the Monte Carlo for the different particle types. The strong 5T target holding field forces low energy charge particles to the direction of the beam. From the Monte Carlo, it is expected that charged particles must have a momentum greater than 100 MeV/c in order to reach the electron arm when it is centered at 30°. The expected trigger rates for different particle types are given in Table 4. The rates in the Cherenkov detector are calculated assuming a threshold of 0.5 to 1 photo-electron which reduces the raw rate of charged pions by a factor of 100 and essentially eliminates the protons and neutrons. The rates in the calorimeter were calculated assuming a 500 MeV threshold on the energy deposited in the calorimeter. Positron to electron singles ratio from the GEANT simulation are shown in Fig. 16, e^+ singles rates is at $< 20\%$ level compare with the e^- rate. In the $(e, e'\pi)$ coincidence events sample, the positron events are easily eliminated when a high momentum hadron is required in coincidence, as has been demonstrated in the CLAS eg1b data analysis.

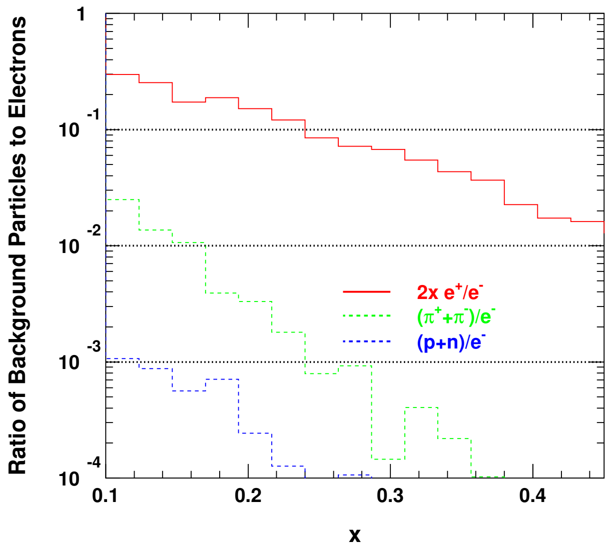

Figure 16: Positron to electron singles ratio in the BigCal according to the GEANT simulation.

Based on the individual detector rates given in Table 4, we expected the rate of true coincidence between the gas Cherenkov and the calorimeter to be 0.97 KHz with an additional accidental rate of 0.32 KHz. The singles rate in the HMS will be below 10 KHz. With a 100 ns coincidence window between the electron arm and the HMS the accidental coincidence rate will be below 1 Hz for the whole 100 ns window. These accidentals can be further reduced by a factor of 10 by a higher cut on the number of photo-electrons in the data analysis and then additional factor of 20 by a 5 ns cut on the coincidence time. The remaining accidental rate should be less than 0.005 Hz under the timing cut.

The coincidence time resolution will be dominated by the timing resolution of the lead glass blocks in BigCal. Experiment 99-007 in Hall A studied the elastic *ep* reaction using a lead glass array with a much larger block size to detect electrons in coincidence with protons which were detected in the Hall A HRS. In Fig. 17, the

	Cherenkov			Calorimeter			
Particle type	e^{+}+e^{-}	$\pi^{+}+\pi^{-}$	Trigger	e^{+}+e^{-}	$\pi^{+}+\pi^{-}$	π^{0}+p+n	Trig
Rate (KHz)	0.79	543.03	6.22	0.66	31.48	228.51	260.65

Table 4: The expected rates for a trigger in the Cherenkov or the calorimeter under assumptions given in the text.

coincidence time spectra for Hall A experiment E99-007 is shown. The resolution in coincidence time has a 3σ of about 3.5 ns.

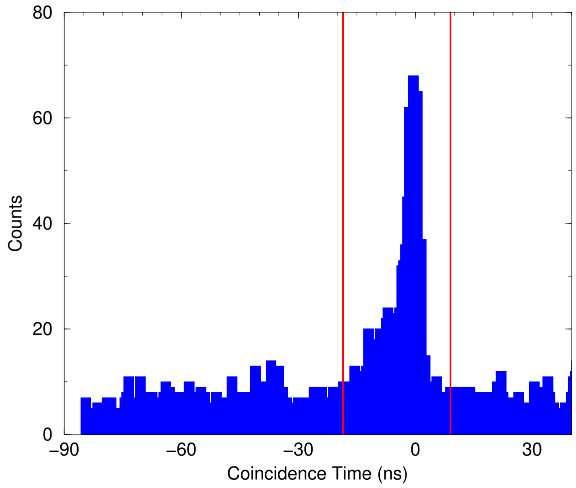

Figure 17: Typical coincidence time-of-flight (TOF) spectra of *ep* elastic scattering in E99-007. The tail to negative TOF is walk in the TDC time due to smaller ADC pulses in the lead glass block. This could have been corrected for, but for the purposes of 99-007 experiment the resolution was adequate.

3.7 Beam line

This experiment will be running with the target field parallel to the beam direction. The effects of the 5T target field on the beam will be minimal. Still the beam is affected by the target field and to insure the incident beam is horizontal at the target, the existing Hall C BE and BZ1 upstream chicane magnets will have to be used to bend the beam slightly upwards before entering the target's magnetic field. For the downstream section of beamline a helium bag will be used to transport the beam to the beam dump.

To maintain the target polarization, the beam has to be rastered. Rastering also insures uniform distribution of heat and radiation on the target material. We would use the slow rastering system developed for previous polarized target experiments in Hall C which produced a 2 cm diameter beam spot at the target. We would also plan to use the same Secondary Emission Beam Position Monitor (SEM) used in previous Hall C experiments.

3.8 The polarized NH_3 and LiD targets

We plan to use the University of Virginia polarized target which has been successfully employed in E143/E155/E155x at SLAC and E93-026 and E01-006 at Jefferson Lab. In this target dynamic nuclear polarization (DNP) is utilized to enhance the low temperature (1K), high magnetic field (5T) polarization of solid materials (here, $^{15}NH_3$ and ^{6}LiD). The irradiation of the target with 140 GHz microwaves drives hyperfine transitions thereby aligning the nucleon spins. Proton polarizations in excess of 95% have been achieved in $^{15}NH_3$ and deuteron polarizations in LiD have have reached maximums of 30% (E155).

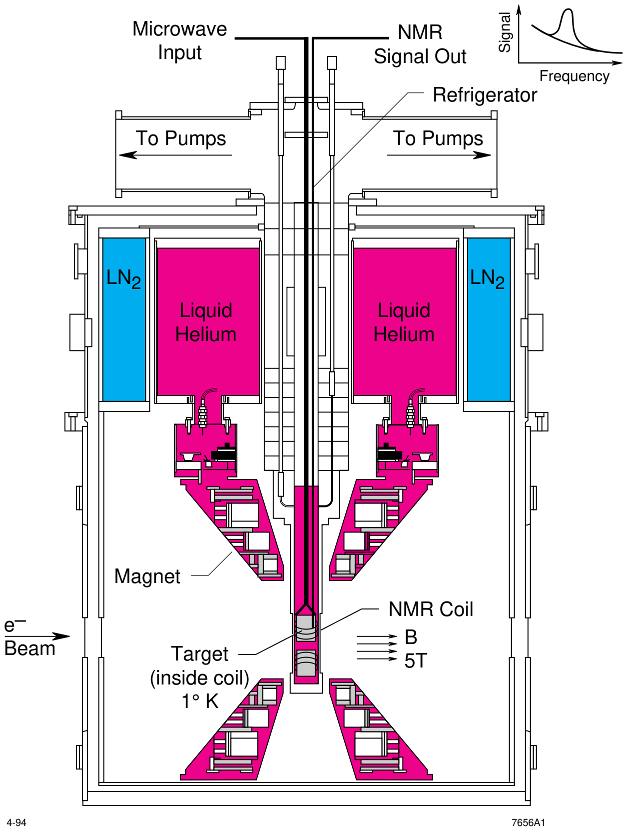

Figure 18: The schematic view of the UVa. polarized target.

A schematic view of the polarized target is shown in Fig. 18. The target magnet coils have a $\pm 50^\circ$ conical shaped aperture along the axis and a $\pm 17^\circ$ wedge shaped aperture along the vertically oriented mid-plane, and this geometry fit our choice of kinematics. The polarized target assembly contains two 2.5 cm diameter, 3 cm long target cells that can be moved by remote control to be located in the uniform field region of the super-conducting Helmholtz pair. The permeable target cells are immersed in a vessel filled with liquid He and maintained at 1 K by use of a high power evaporation refrigerator.

Both beam heating and radiation damage from the electron beam reduce the in-beam average polarizations which we have taken to be 80% for the NH_3 target and 20% for the LiD target. (The average in-beam polarization of LiD during E155 was 22%.) Most of the radiation damage is repaired by annealing the target at about 80 K (for NH_3), until the accumulated dose reaches $> 2 \times 10^{17}$ electrons, at which point the material needs to be replaced. LiD suffers much less from radiation damage which is repaired similarly, but at a temperature of 185 K.

We have included the overhead time for target annealing in our beam request. Most of the overhead time can be shared with other activities, for example Möller runs, and unpolarized target runs.

The 3 cm NH_3 target corresponds to 1.8 g/cm^2 of material. An average beam current of 100 nA was achieved in earlier JLab experiments. The luminosity corresponding to the polarized proton in the uniform field region is 80×10^{33} cm^{-2} sec^{-1}. The spin dilution factor, which is the fraction of polarizable nucleons in the target, will be about 0.15 for NH_3, assuming that 60% of the target cup contains NH_3, with the remaining volume filled with He. The NH_3 target is about 0.04 r.l. in thickness.

The 3 cm long ^{6}LiD target corresponds to about 1.6 g/cm^2 of material, and is about 2% of a radiation length. Various studies have shown that, to a good approximation, ^{6}Li acts as a polarized proton and a polarized neutron plus an unpolarized spectator particle [52]. This results in a spin dilution factor of $\simeq 0.5$ (compared to 0.28 for ND_3). Even after taking into account target windows and liquid helium, $s_f \simeq 0.4$, and in conjunction with its high polarization, ^{6}LiD gives a much higher nucleon average polarization than any other solid target. ^{6}LiD polarized targets have been successfully used by the University of Virginia group to measure g_1 and g_2 at SLAC [53] and is being used by COMPASS.

LiD has other advantages over ND_3 including the fact that the polarization can be measured with better accuracy. This lies in the fact that the NMR signal of ND_3 has a poorer S/N ratio as there is a splitting of the RF transitions arising from the interaction of the quadrupole moment of the deuteron with an electric field gradient in the crystal. There exists no such interaction (no electric field gradient in the LiD crystal) in LiD and the single NMR peak is much narrower and better defined.

The third advantage of LiD is a greater tolerance to radiation (mentioned above and better by a factor of 5) over ND_3, resulting in fewer anneals and a greater data taking efficiency. ^{6}LiD, like ND_3, must be pre-irradiated to create the paramagnetic centers necessary for DNP.

The target polarization will be measured continuously via NMR using a coil embedded in the target material coupled to the Liverpool Q-meter and RF processing module. This system has been the de-facto standard in polarized targets for the last 20 years and has been successfully employed by the UVA group in a series of experiments at SLAC and JLAB.

The response of the NMR circuit must be calibrated against a known polarization - the thermal equilibrium polarization present in a spin system in equilibrium with the environment. These calibrations, known as TE measurements, are a critical part of any polarized target experiment and can be time-consuming, especially with LiD which has a long relaxation time. Typically TE measurements are done at the beginning of the run, before and after any configuration changes to the target and opportunistically, at any sustained interruption in the delivery of beam. We have included in the run plan time for TEs interspersed during the run.

The ^{6}Li polarization in ^{6}LiD was studied at SLAC [54] and found to follow the prediction of equal spin temperatures (EST) based on a measurement of the deuteron polarization. It will be monitored. As part of the program to minimize the sources of systematic errors, the target polarization direction will be reversed after each anneal by adjusting the microwave frequency.

In order to determine accurately the A-dependence from the various nuclei in the polarized target, a small amount of beam time will be used to measure the rates from auxiliary targets consisting primarily of helium, beryllium or carbon, and aluminum. These targets will also allow a measurement of the dilution factor for the polarized targets. These runs are often done in coordination with the annealing sequence when the target is warmed up and the polarizable targets do not have to be in the beam line.

3.9 Effects of the longitudinal target field

The polarized target has been used at several experiments at JLab and the reconstruction of target angles and positions with the target field has been well understood. In addition, the acceptance of the HMS has also been well understood in single arm inclusive experiments. The longitudinal field of the polarized target will effect the trajectories of outgoing charged particles. Of importance for this experiment is the opposite effect the target field will have on trajectories of positive and negative particles into the HMS. For this experiment, we will measure $^{12}\mathrm{C}(e,\pi^{\pm})$ reaction with target field turned on and off to understand the relative acceptances for $\pi^{\pm}$ that are needed for making the combined asymmetries $A_{1N}^{\pi^+\pm\pi^-}$, as has been during E01-006. In the left panel of Fig. 19, a comparison is made between the measured rates of ^{12}C(e,e$'$) reaction to a Monte Carlo simulation. The data was taken at a beam energy of 5.7 GeV and the HMS angle of 13.15° with the target field parallel to the beam direction.

The difference of the HMS acceptance between positively and negatively charged particles when the target field turned on is shown in the right panel of Fig. 19. The angular acceptance is plotted for the 2.71 GeV/c HMS setting. XPTAR is the charge particle's original out-of-plane angle (+XPTAR for trajectory downwards) and YPTAR is the in-plane angle. For no target field, the acceptance is shown by the green line. With the target field on, the acceptance for positively (negatively) charged particles is shown by the black (red) line. There is a symmetric shift in the acceptance with the centroid in XPTAR shifted by -20 mrad (-1.2°) for negative particles and with the opposite sign for positive charge.

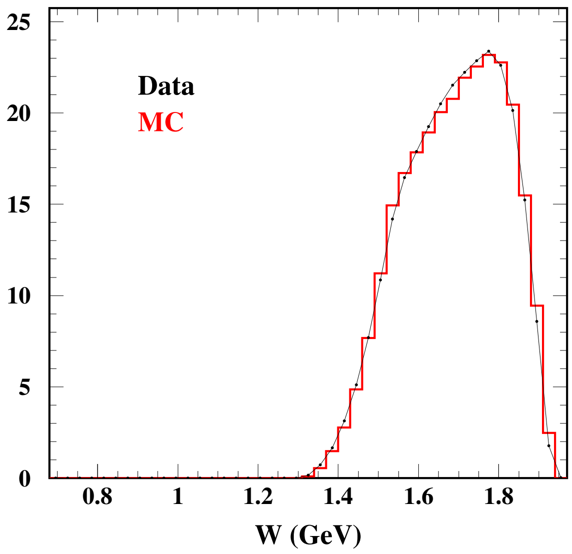

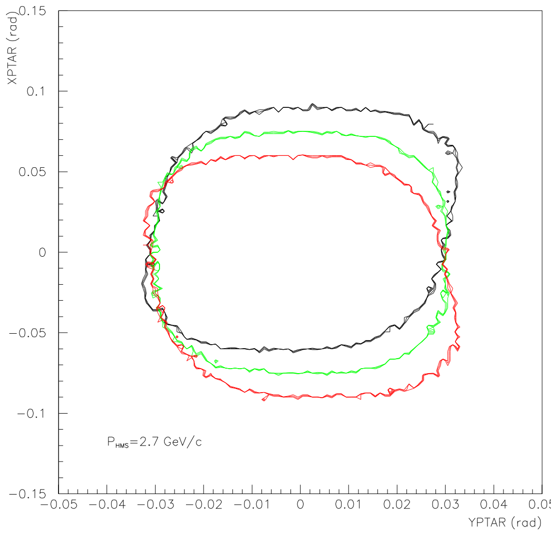

Figure 19: Left panel: a comparison between rates for the ^{12}C(e,e$'$) reaction from E01-006 data and a Monte Carlo simulation as a function of W. Right panel: the HMS acceptance in XPTAR (hadron's original out-of-plane angle) vs YPTAR (in-plane angle) for π^+ (black line) is compared with π^- (red line) for this experiment, the HMS acceptance corresponding to target field off (green line) is also shown.

4 Event Rate Estimate and the Expected Raw Asymmetries

4.1 Cross section and rate estimate

The estimation of the coincidence cross sections has the following inputs:

- The inclusive $p(e,e')$ and $d(e,e')$ cross sections. Deep-inelastic cross section for ^{6}Li, ^{4}He, ^{12}C and ^{14}N are assumed to be the sum of the protons and the neutrons, neglecting the nuclear effects.
- Parameterizations of the fragmentation functions D_π^+, D_π^- and D_s^π for quark to pion fragmentation, D_K^+, D_K^- and D_d^K for quark to kaon fragmentation.
- A model of the transverse momentum distributions of pion and kaon as fragmentation products.

The inclusive deep inelastic (e,e') cross section can be expressed in the quark parton model as:

$$\frac{d^2\sigma}{d\Omega dE'} = \frac{\alpha^2(1+(1-y)^2)}{sxy^2}\frac{E'}{M_N\,\nu}\sum_{q,\bar{q}} e_q^2 f_1^q(x), \tag{35}$$

where $s = 2E\,M_N + M_N^2$. The unpolarized quark distribution functions $f_1^q(x)$ and $f_1^{\bar{q}}(x)$ are taken from the CTEQ5M global fits [55]. The semi-inclusive $(e,e'h)$ cross section relates to the quark fragmentation function $D_q^h(z)$ and the total inclusive cross section σ_{tot} through:

$$\frac{1}{\sigma_{tot}} \frac{d\sigma(e, e'h)}{dz} = \frac{\sum_{q,\bar{q}} e_q^2 f_1^q(x) D_q^h(z)}{\sum_{q,\bar{q}} e_q^2 f_1^q(x)}. \tag{36}$$

For the quark to pion fragmentation functions $D_\pi^+(z)$ and $D_\pi^-(z)$, close to $Q^2 = 2.5$ GeV^2, we follow the parameterization of Kretzer, Leader and Christova [56]:

$$\begin{aligned} D_\pi^+(z) &= 0.689 z^{-1.039}(1-z)^{1.241} \\ D_\pi^-(z) &= 0.217 z^{-1.805}(1-z)^{2.037} \end{aligned} \tag{37}$$

For the fragmentation functions D_s^π, D_K^+, D_K^- and D_d^K we follow the parameterization [26] of BKK.

Existing data indicate that the fragmented products follow a Gaussian-like distribution in transverse momentum. For the $N(e, e'\pi)X$ reaction, recent HERMES preliminary data[57] showed that the transverse momentum ($P_\perp$) distribution for both π^+ and π^- follow the form of $e^{(-aP_\perp^2)}$ with $a = 3.76$ (GeV/c)$^{-2}$, corresponding to an average quark transverse momentum of $\langle P_\perp^2 \rangle = 0.26$ (GeV/c)^2. Charge kaon transverse momentum distributions are also found to be similar [57]. We used this distribution and realistic spectrometer acceptances in a Monte Carlo simulation to estimate the count rates. The issue of hadron decay is also considered in the rate estimation. The typical survival factors for $\pi^\pm$ and $K^\pm$ of 2.71 GeV/c momentum are 0.85 and 0.29 correspondingly, after a flight-path of 26.0 m in HMS.

4.2 The expected raw asymmetries and the statistical uncertainties

The event rates, total number of events in each bin, the expected raw online asymmetries and the associated statistical uncertainties for the nominal kinematics bins are listed in Table–5 for the $(e, e'\pi)$ and $(e, e'K)$ reactions. Charged kaon yields are expected to be at the 10% $\sim$ 20% level compared to the yields of pion. Therefore, kaon asymmetries will also be determined with reasonable accuracy. We have assumed a beam current of 80 nA, beam polarization of 80%, target thickness of 3 cm, a polarization of 80% for the NH_3 target and 20% for the LiD target.

The expected statistical uncertainties of A_{1N}^h and $A_{1p}^{h+\bar{h}}$ are listed in Table 6 and Table 7 . The expected statistical uncertainties of $A_{1p}^{\pi^+-\pi^-}$ and $A_{1d}^{\pi^+-\pi^-}$ are listed in Table 8 together with the uncertainties of the extracted polarized parton distribution according to the Christova-Leader (CL) method. Part of the systematic uncertainties due to the knowledge [58,9] of $g_1^p(x)$ and $g_1^n(x)$ ($\delta g_1^p = 0.0059$, $\delta g_1^n = 0.0057$) are also included in obtaining $\delta(x(\Delta\bar{u} - \Delta\bar{d}))_{LO}$ in Table 8. The approved SANE experiment in Hall C is expected to improve the world knowledge of $g_1^p(x)$ significantly. The inclusive data from this experiment will also provide a high statistical data set for extracting $g_1^p(x)$.

Pion rates and the total number of events on the NH_3 target:

$\langle x \rangle$	$\langle z_\pi \rangle$	R^{π^+} Hz	R^{π^-} Hz	N^{π^+} k	N^{π^-} k	$f^\pi P_B P_T \mathcal{P}_{kin}$ π^+	π^-	$\delta A_\parallel^{\pi^+}$ %	$\delta A_\parallel^{\pi^-}$ %
0.122	0.52	0.53	0.33	280	93	0.15	0.13	0.19	0.33
0.203	0.56	0.41	0.21	214	60	0.14	0.11	0.22	0.41
0.298	0.61	0.26	0.12	138	33	0.13	0.10	0.27	0.54
0.413	0.67	0.12	0.05	63	13	0.12	0.09	0.40	0.86

Pion rates the total number of events on the LiD target:

$\langle x \rangle$	$\langle z_\pi \rangle$	R^{π^+} Hz	R^{π^-} Hz	N^{π^+} k	N^{π^-} k	$f^\pi P_B P_T \mathcal{P}_{kin}$ π^+	π^-	$\delta A_\parallel^{\pi^+}$ %	$\delta A_\parallel^{\pi^-}$ %
0.122	0.52	0.85	0.54	578	184	0.09	0.09	0.13	0.23
0.203	0.56	0.64	0.35	434	119	0.08	0.08	0.15	0.29
0.298	0.61	0.40	0.20	276	66	0.07	0.07	0.19	0.39
0.413	0.67	0.18	0.08	124	26	0.06	0.06	0.28	0.61

Kaon rates and the total number of events on the NH_3 target:

$\langle x \rangle$	$\langle z_K \rangle$	R^{K^+} Hz	R^{K^-} Hz	N^{K^+} k	N^{K^-} k	$f^K P_B P_T \mathcal{P}_{kin}$ K^+	K^-	$\delta A_\parallel^{K^+}$ %	$\delta A_\parallel^{K^-}$ %
0.122	0.52	0.09	0.05	45	13	0.14	0.13	0.47	0.86
0.203	0.57	0.06	0.03	33	7	0.14	0.12	0.55	1.12
0.298	0.62	0.04	0.01	21	3	0.13	0.11	0.69	1.58
0.413	0.68	0.02	-	9	-	0.12	-	1.01	-

Kaon rates and the total number of events on the LiD target:

$\langle x \rangle$	$\langle z_K \rangle$	R^{K^+} Hz	R^{K^-} Hz	N^{K^+} k	N^{K^-} k	$f^K P_B P_T \mathcal{P}_{kin}$ K^+	K^-	$\delta A_\parallel^{K^+}$ %	$\delta A_\parallel^{K^-}$ %
0.122	0.52	0.14	0.08	93	26	0.09	0.09	0.33	0.61
0.203	0.57	0.10	0.05	67	15	0.08	0.08	0.38	0.80
0.298	0.62	0.06	0.02	42	7	0.07	0.07	0.49	1.14
0.413	0.68	0.03	-	19	-	0.06	-	0.72	-

Table 5: Pion and kaon event rates (R^h), the total number of events (N^h), the product of kinematic factor, beam and target polarization and the dilution factor ($f^h P_B P_T \mathcal{P}_{kin}$), the expected statistical uncertainties of the raw asymmetry ($\delta A_\parallel^h$) are listed for both the NH_3 and the LiD targets. Data of all x-bins will be collected simultaneously.

$\langle x \rangle$	$\delta A_{1p}^{\pi^+}$ %	$\delta A_{1p}^{\pi^-}$ %	$\delta A_{1d}^{\pi^+}$ %	$\delta A_{1d}^{\pi^-}$ %	$\delta A_{1p}^{K^+}$ %	$\delta A_{1p}^{K^-}$ %	$\delta A_{1d}^{K^+}$ %	$\delta A_{1d}^{K^-}$ %
0.122	1.27	2.58	1.48	2.63	3.25	6.59	3.69	6.91
0.203	1.54	3.59	1.92	3.66	4.02	9.38	4.87	10.19
0.298	2.03	5.40	2.71	5.52	5.30	14.02	6.92	16.29
0.413	3.19	9.99	4.54	9.84	8.27	-	11.56	-

Table 6: The expected statistical uncertainties of the double-spin asymmetry A_{1N}^h.

$\langle x \rangle$	$\delta A_{1p}^{\pi^+ + \pi^-}$ %	$\delta A_{1d}^{\pi^+ + \pi^-}$ %	$\delta A_{1p}^{K^+ + K^-}$ %	$\delta A_{1d}^{K^+ + K^-}$ %
0.122	1.23	1.37	3.13	3.44
0.203	1.54	1.80	3.94	4.62
0.298	2.07	2.57	5.25	6.67
0.413	3.31	4.34	8.24	-

Table 7: The expected statistical uncertainties of the combined double-spin asymmetry $A_{1N}^{h+\bar{h}}$.

$\langle x \rangle$	$\delta A_{1p}^{\pi^+ - \pi^-}$ %	$\delta A_{1d}^{\pi^+ - \pi^-}$ %	$\delta(x\Delta u_v)_{CL}$	$\delta(x\Delta d_v)_{CL}$	$\delta(x(\Delta\bar{u} - \Delta\bar{d}))_{LO}$
0.122	4.14	6.26	0.021	0.049	0.024
0.203	3.89	6.27	0.023	0.055	0.028
0.298	4.30	7.40	0.024	0.057	0.029
0.413	5.81	10.80	0.024	0.056	0.030

Table 8: The expected uncertainties of $A_{1p}^{\pi^+ - \pi^-}$ and $A_{1d}^{\pi^+ - \pi^-}$ and the extracted polarized parton distribution according to the Christova-Leader (CL) method. Uncertainties of $\delta g_1^p = 0.0059$ and $\delta g_1^n = 0.0057$ are also included in obtaining $\delta(x(\Delta\bar{u} - \Delta\bar{d}))_{LO}$.

Systematic uncertainty of A_{1N}^h and $A_{1N}^{\pi^+ \pm \pi^-}$

Knowledge of target polarization and dilution factor dominates the systematic uncertainty of A_{1N}^h. The effects of radiative corrections will be treated in a Monte Carlo simulation following the procedures of the HERMES analysis [2], which found that the systematic uncertainties introduced by this procedure are negligible. Kinematic smearing will also be treated following the procedure of the HERMES analysis.

Since the direction of $\vec{q}$ is close to the beam direction, the effects caused by the small transverse component of the target polarization relative to $\vec{q}$ can be safely ignored. The size of the transverse double-spin asymmetry A_{2N}^h is expected to be much small compare with A_{1N}^h and it is weighted by the hadron transverse momentum p_t, being further suppressed in this experiment.

Major systematic uncertainties in double-spin asymmetries A_{1N}^h:

Uncertainty in target polarization $\delta P_T/P_T$:	$\pm 2.5\%$ relative
Uncertainty in beam polarization $\delta P_B/P_B$:	$\pm 2.0\%$ relative
Helicity correlated beam charge uncertainty $\delta(Q_+/Q_-)$:	$\ll 10^{-4}$ absolute
Radiative correction and smearing:	$\pm 1.5\%$ relative
Dilution factor $\delta f/f$:	$\pm 2.5\%$ relative
Total systematic uncertainty of A_{1N}^h	$\pm 4.3\%$ **relative**

The systematic uncertainties of $A_{1N}^{\pi^+ \pm \pi^-}$ are propagated from $A_{1N}^{\pi^+}$ and $A_{1N}^{\pi^-}$ while assuming a systematic uncertainty of $\delta r/r = 2.0\%$ in Eq. 33.

Systematic uncertainty of Δq

The consistency of Δq obtained from several independent methods of flavor decomposition will serve as the cross-checks of the systematic uncertainties in this experiment. The HERMES analysis shown that the uncertainties in the fragmentation function dominated the systematic uncertainties in the flavor decomposition of the LO purity method, introducing uncertainties of $0.02 \sim 0.06$ in the value of the extracted $\Delta u/u$ and $\Delta d/d$. The uncertainties introduced by the unpolarized PDFs and R are found to be very small. Since we will only need the ratios of the fragmentation functions as inputs for flavor decomposition, we would expect a smaller systematic uncertainties compared to that of the HERMES analysis.

In principle, intermediate ρ production processes are part of the fragmentation process and should not subtracted from the SIDIS cross sections. Furthermore, due to the charge conjugation, the effect of intermediate ρ^0 production is canceled in observables related to $\pi^+ - \pi^-$. Therefore, the Christova-Leader method of flavor decomposition is not sensitive to ρ production. Calculations of the yield of $(e, e'\pi)$ from intermediate ρ production have been done in the same Monte Carlo used for SIDIS reaction. The cross section for $N(e, e'\rho^\circ)X$ was calculated from a modified version of the formalism used in PYTHIA [59]. For π^+ production, the yield $(e,e')\pi^\pm$ from ρ is about 13%. In Fig. 20, the distribution of π yield versus four kinematic variables: W', z, P_t and ϕ_{pq} are shown. The red line is the yield from ρ production while the black line is the total combined yield from SIDIS and ρ production. One can see that shapes of the distributions are similar for both pions for ρ production and pions from SIDIS.

At a high-z setting of this experiment ($z \simeq 0.5 \sim 0.6$), target fragmentation contamination is expected to be small, as has been shown by the HERMES LUND based Monte Carlo simulation. In addition, in the $\pi^+ - \pi^-$ yield target fragmentation contributions are mostly canceled.

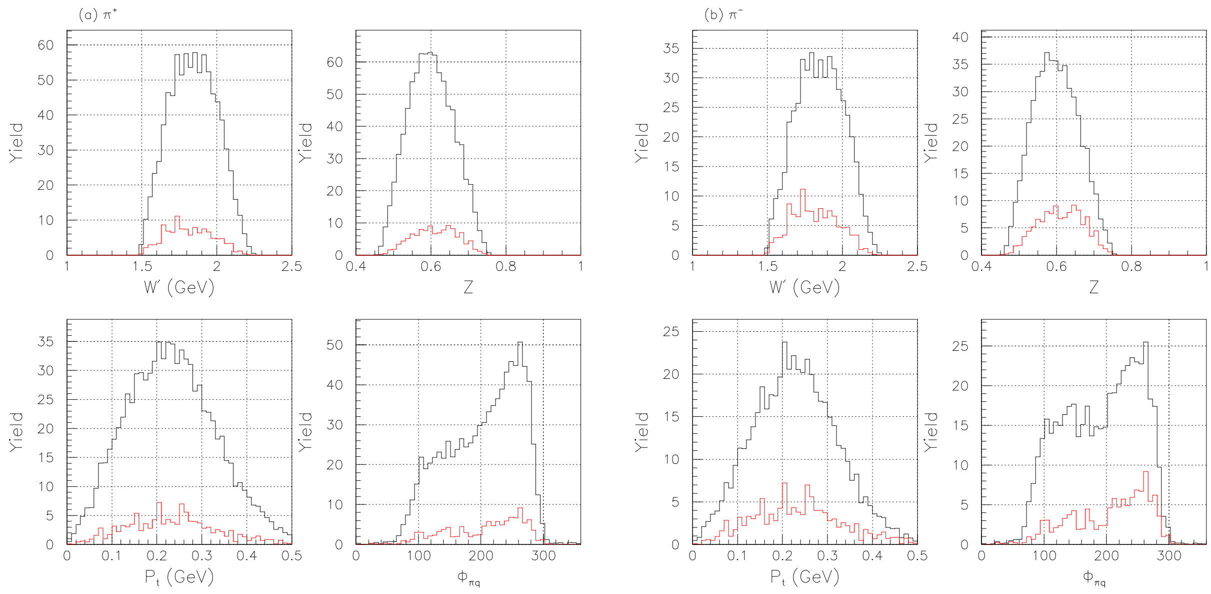

Figure 20: Comparison of the yield (in arbitrary units) of $(e,e'\pi)$ from intermediate ρ production (red line) to the total combined yield from DIS and ρ production (black line) for the $x = 0.203$ bin. The left figure is for π^+ and the right figure is for π^- production.

5 Beam time request

The beam time request are listed in detail in Table 9. The relative time between h^+ and h^- runs are chosen to minimize the uncertainty of $A_{1N}^{\pi^+-\pi^-}$ for the $x = 0.203$ bin. The time allocations for NH_3 and LiD targets are chosen to minimize the uncertainty of $\Delta u_v - \Delta d_v$ according to Eq. 18. We request 600 hours (25 days) of beam time in total, of which 510 hours is for beam on the polarized target. A large amount of overhead time (90 hours total) is requested mostly for target related activities. This overhead time can be shared with other experimental activities, such as Möller measurements and unpolarized target measurements, as has been done in the past during other Hall C polarized target experiments. Major target changes can also be arranged to coincide with the scheduled accelerator maintenance activities in order to save overhead time.

P_{HMS}	NH_3 target		LiD target	
GeV/c	Time-h^+ hour	Time-h^- hour	Time-h^+ hour	Time-h^- hour
2.710	**146**	**79**	**190**	**95**
Beam on polarized targets	**510**			
Target overhead, Möller runs and ^{12}C target runs.	**90**			
Total Time Request	**600 (25 days)**			

Table 9: Details of the beam time request.

In addition to the main proposal, we also request permission for parasitic data taking during half the time (50 hour) of the 6.0 GeV longitudinal target runs of the "SANE" experiment to test the semi-inclusive spin-duality in deep-inelastic $\vec{p}(\vec{e}, e'\pi^+)X$ reaction. A detailed parasitic run plan, a kinematics table and a Monte Carlo simulation of phase space coverage are attached in Appendix–C. The parasitic data taking also serves as instrumentation shake-down for this experiment. If scheduled to run next to each other, the change-over time needed between the SANE experiment and this experiment should be less than one day.

6 The Expected Results

6.1 Double spin asymmetries A^h_{1N} and $A^{\pi^+\pm\pi^-}_{1N}$

The expected statistical accuracies of semi-inclusive double-spin asymmetries $A^{\pi^+}_{1p}$, $A^{\pi^-}_{1p}$, $A^{\pi^+}_{1d}$ and $A^{\pi^-}_{1d}$ are shown in Fig. 21 as functions of x. Systematic uncertainties of $\pm 4.3\%$ relative to the asymmetries are not shown. HERMES and SMC data are also plotted as a comparison. The CLAS eg1b $A^{\pi^+}_{1p}$ preliminary results[5] , at $E_0 = 5.7$ GeV $\langle Q^2 \rangle = 1.77$ GeV^2 and a cut of $W' > 1.1$ GeV, are also plotted. The expected kaon asymmetries are shown in Fig. 22 for the proton and the deuteron.

The expected statistical accuracies of the combined charge pion asymmetries $A^{\pi^+ + \pi^-}_{1p}$, $A^{\pi^+ - \pi^-}_{1p}$, $A^{\pi^+ + \pi^-}_{1d}$ and $A^{\pi^+ - \pi^-}_{1d}$ are shown in Fig. 23. The SMC asymmetries of h^+ and h^- have been naively combined to illustrate the improvements of this experiment on the statistical accuracies. This naive-combination of SMC data assumes $\langle z \rangle = 0.5$ and ignores differences in phase spaces.

6.2 Flavor decomposition of quark polarization

The expected statistical accuracies of $x\Delta u_v$, $x\Delta d_v$ and $x(\Delta\bar{u} - \Delta\bar{d})$ are shown in Fig. 24 for the "fixed-z purity" method and the Christova-Leader method. Only the

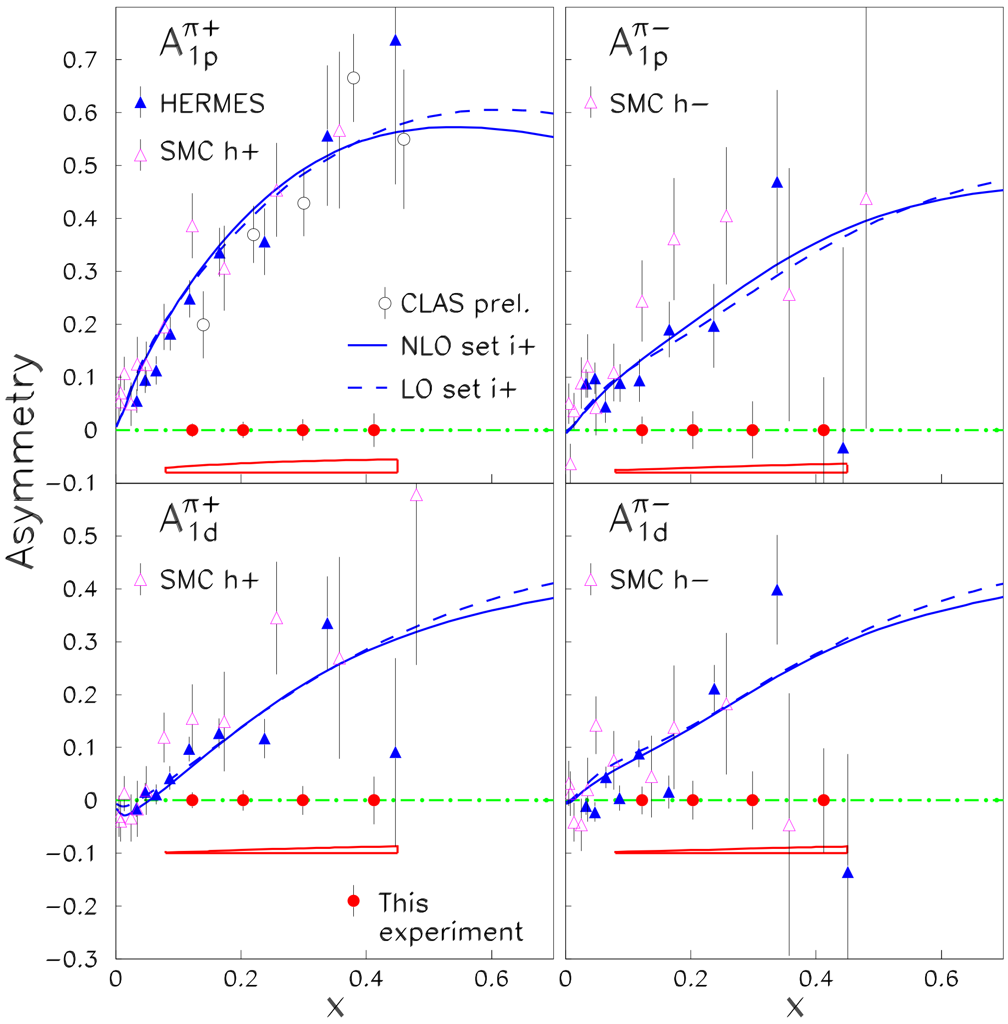

Figure 21: The expected statistical accuracy of pion semi-inclusive physics asymmetries $A_{1p}^{\pi^+}$, $A_{1p}^{\pi^-}$, $A_{1d}^{\pi^+}$ and $A_{1d}^{\pi^-}$ as functions of x. The HERMES charged pion results [2] and the SMC charged hadron results [4] are shown. The preliminary CLAS eg1b results [5] of $A_{1p}^{\pi^+}$ are shown to agree with the existing SIDIS data. The next-to-leading-order (solid lines) and the leading order (dashed lines) predictions [19] using de Florian and Sassot's parton distributions [16] set $i+$ are plotted for $\langle Q^2 \rangle = 2.5$ GeV^2 and $\langle z \rangle = 0.5$. The expected systematic uncertainties of this experiment are shown at the bottom of each panel.

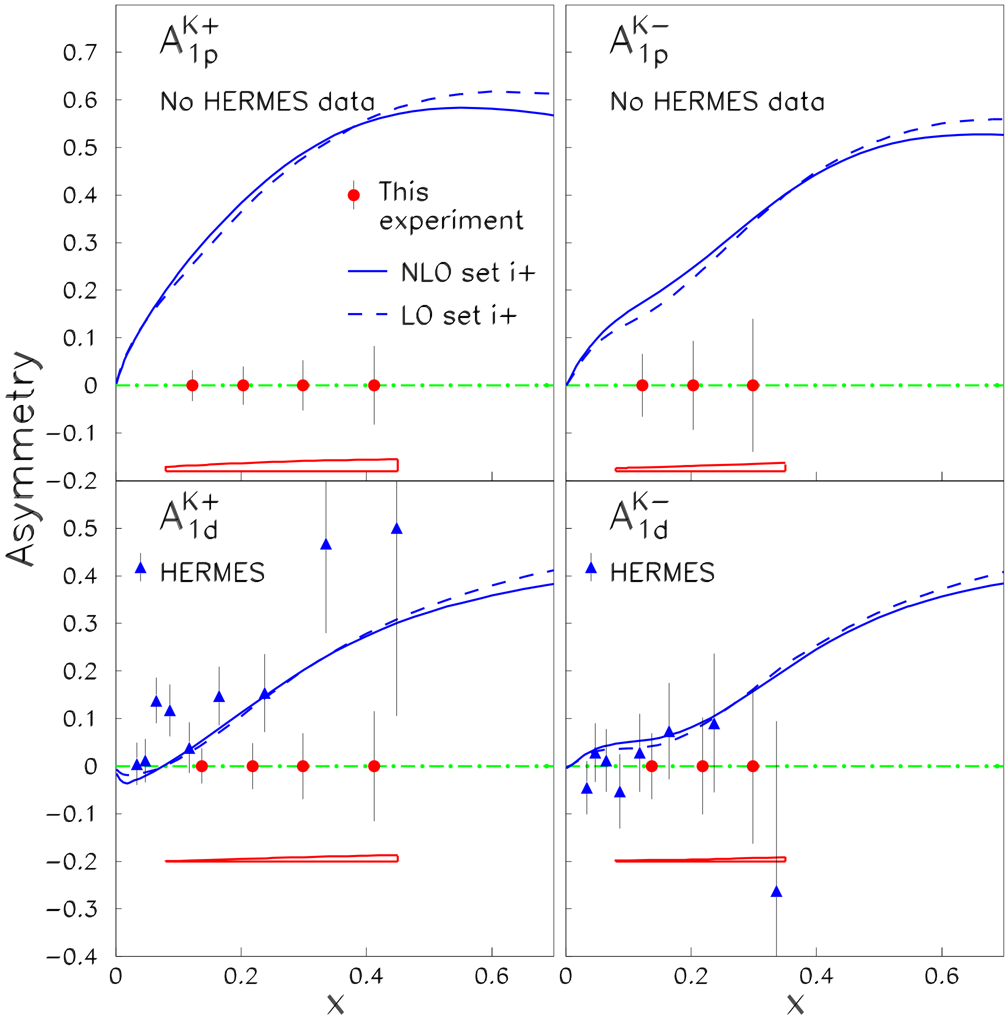

Figure 22: The expected statistical accuracy of kaon semi-inclusive physics asymmetries $A_{1p}^{K^+}$, $A_{1p}^{K^-}$, $A_{1d}^{K^+}$ and $A_{1d}^{K^-}$ as functions of x. HERMES results [2] on the deuteron target are also shown. The HERMES proton data were collected before the installation of the RICH detector and the kaon asymmetries are not available. The next-to-leading-order (solid lines) and the leading order (dashed lines) predictions [19] using de Florian and Sassot's parton distributions [16] set $i+$ are plotted for $\langle Q^2 \rangle = 2.5$ GeV^2 and $\langle z \rangle = 0.5$. The expected systematic uncertainties of this experiment are shown at the bottom of each panel.

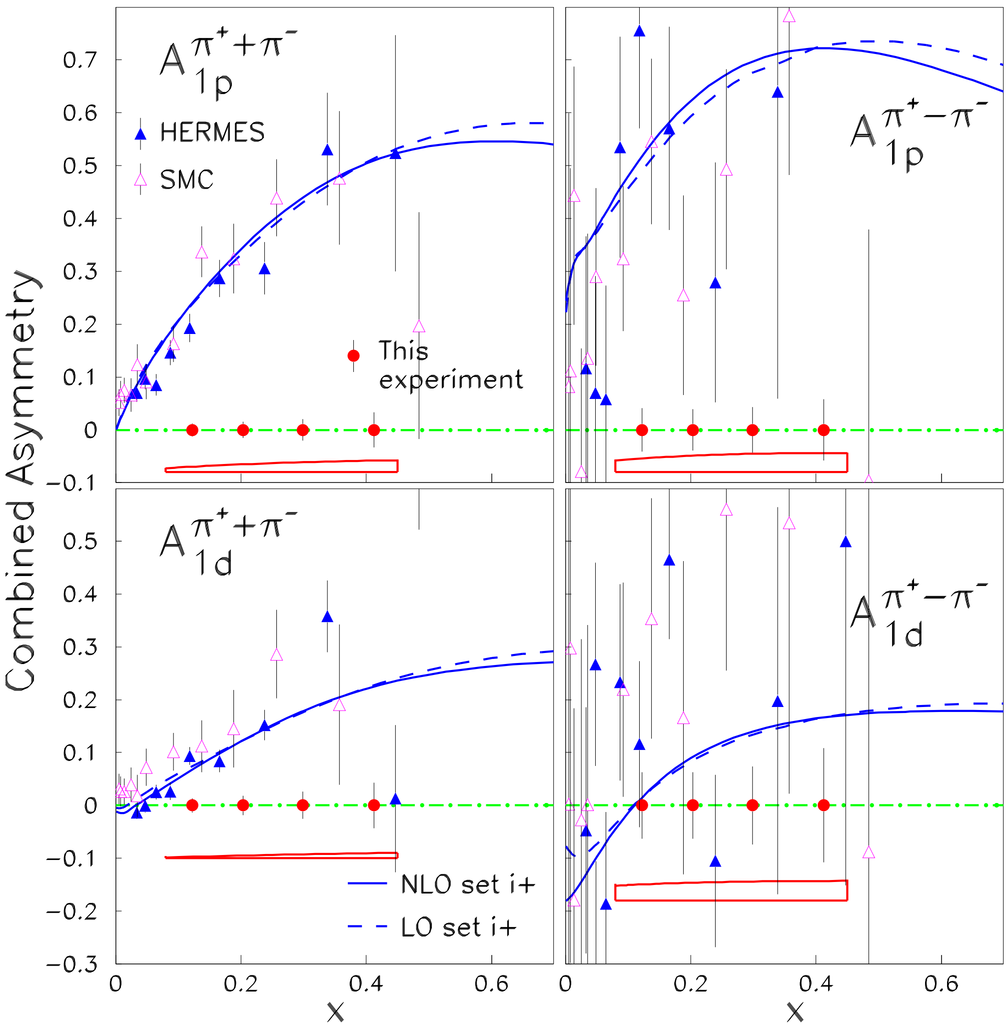

Figure 23: The expected statistical accuracy of the combined asymmetry $A_{1p}^{\pi^+ + \pi^-}$, $A_{1p}^{\pi^+ - \pi^-}$, $A_{1d}^{\pi^+ + \pi^-}$ and $A_{1d}^{\pi^+ - \pi^-}$. The next-to-leading-order (solid lines) and the leading order (dashed lines) predictions[19] using de Florian and Sassot's parton distributions[16] set $i+$ are plotted for $\langle Q^2 \rangle = 2.5$ GeV^2 and $\langle z \rangle = 0.5$.

expected systematic uncertainties of Christova-Leader method are plotted in Fig. 24. The individual quark polarization distributions extracted from the "fixed-z purity" method are shown in Fig. 25. The expected results of $\Delta u/u$ and $\Delta d/d$ are compared with HERMES preliminary results and the recent Hall A results in Fig. 26. At the high-x bins, this experiment overlaps with the recent Hall A experiment [9] (E99117) which extracted ratios of $\Delta u/u$ and $\Delta d/d$ from the inclusive asymmetry A_{1n} at high-x. The consistency check between the semi-inclusive data from this experiment and the inclusive data of E99117 provides the validity test of the various flavor decomposition methods in semi-inclusive experiments. The statistical accuracies in the light sea flavor asymmetry are shown in Fig. 27. Clearly we will have enough sensitivity to rule out some of the theory models listed in Table. 1.

7 Relation with other experiments

- HERMES is now concentrating on transverse polarized data taking to measure the transversity of the proton. There's no plan to take more longitudinal polarized target data.

- Hall B polarized target data were originally collected for inclusive measurements in order to extract A_{1p} and A_{1d}. Part of data taken in year 2000 with 5.7 GeV beam (EG1b) can be analyzed for $(e, e'\pi)$ reactions. However, the physics goals addressed in this proposal can not be achieved in analyzing the existing EG1b data. The much higher luminosity, the much better coverage in deep inelastic kinematics, and the precision knowledge on acceptance, particle identification and detector efficiency make this proposal unique at Jefferson Lab.

  At 6 GeV beam energy, to keep Q^2 and W as high as possible in order to access the deep-inelastic region, the direction of momentum transfer $\vec{q}$ must be kept very close to the direction of the beam, typically to within 10°. Therefore, very forward-angle hadron detection is crucial in order to detect the leading hadrons in the fragmentation and to have a clear separation between the current fragmentation and the target fragmentation regime. In addition, a cut in W' as high as possible is desired in order to access the deep inelastic region and to avoid the exclusive channels and the resonance production channels. While Hall C HMS can reach 10.8°, the nominal CLAS acceptance shrinks rapidly for hadrons coming out at angles less than 20°.

  At hadron momentum larger than 1.5 GeV/c, the CLAS particle ID becomes problematic, especially for kaons. Kaon contamination in the A_{1p}^{π} asymmetry can not be avoided. In addition, since positively charged and negatively charged hadrons are bent in opposite directions, differences in the phase spaces and the detection efficiencies are expected, it is difficult to construct the combined $\pi^+ \pm \pi^-$ asymmetries from the existing EG1b data.

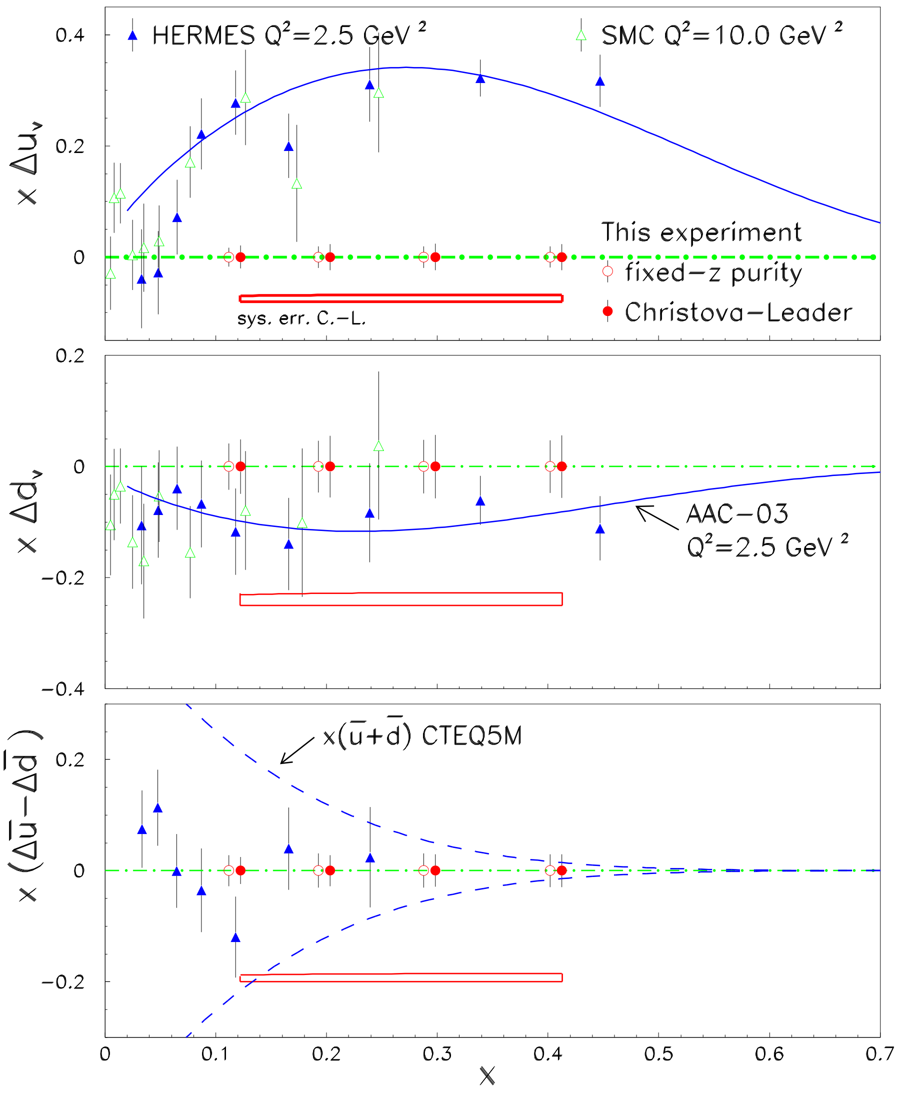

Figure 24: The statistical accuracies for two independent methods of flavor decomposition (Christova-Leader and "fixed-z purity") are compared with the HERMES data [3] and the SMC data [4]. The open box represents the systematic uncertainties of the Christova-Leader method.

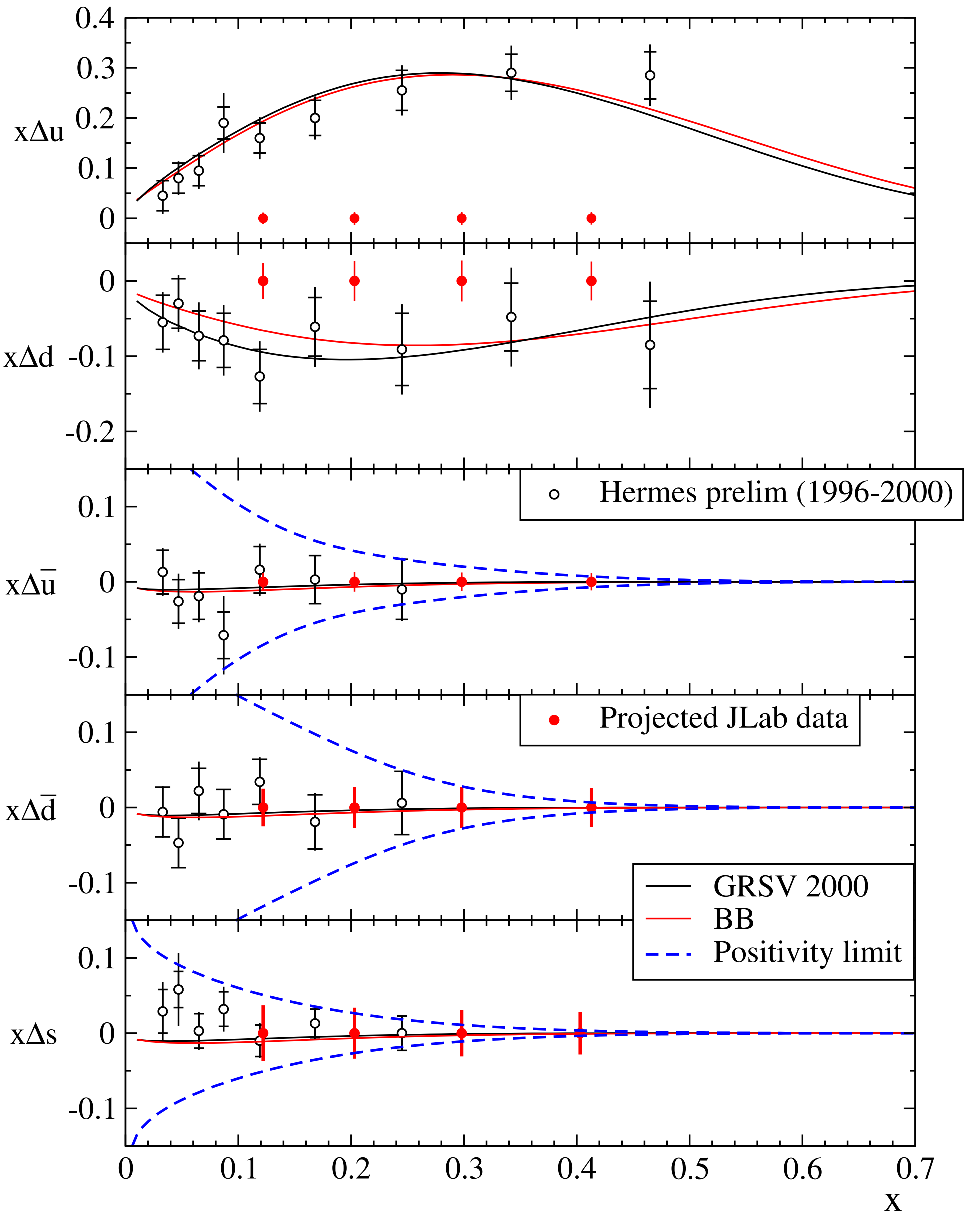

Figure 25: The expected statistical accuracy of 5-flavor decomposition compared with the preliminary HERMES data (1996-2000). The error bars on the projected JLab data are statistical only while the HERMES data includes both statistical (inner bars) and the systematic errors.

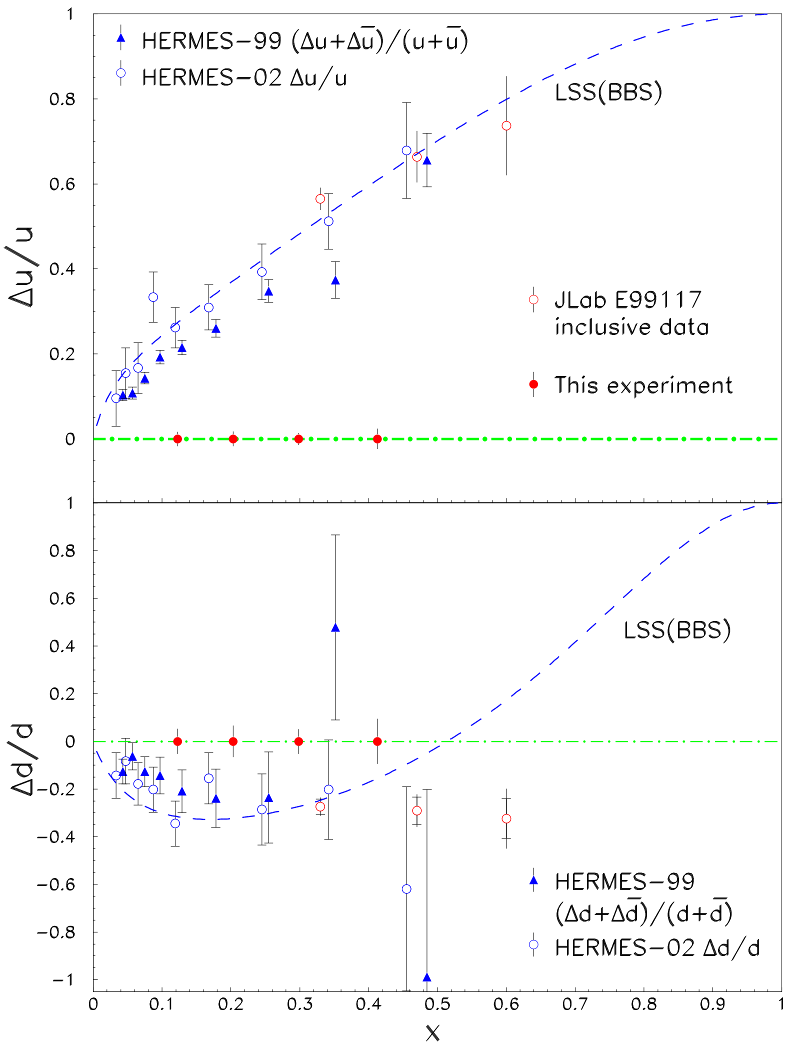

Figure 26: The expected statistical accuracy of $\Delta u/u$ and $\Delta d/d$ compared with the HERMES data[3] (1996-2000) and the earlier published HERMES data (HERMES-99). The error bars on the projected JLab data are statistical only while the HERMES data includes both statistical (inner bars) and the systematic errors. The Hall A inclusive results[9] from polarized ^{3}He target (E99117) are also shown.

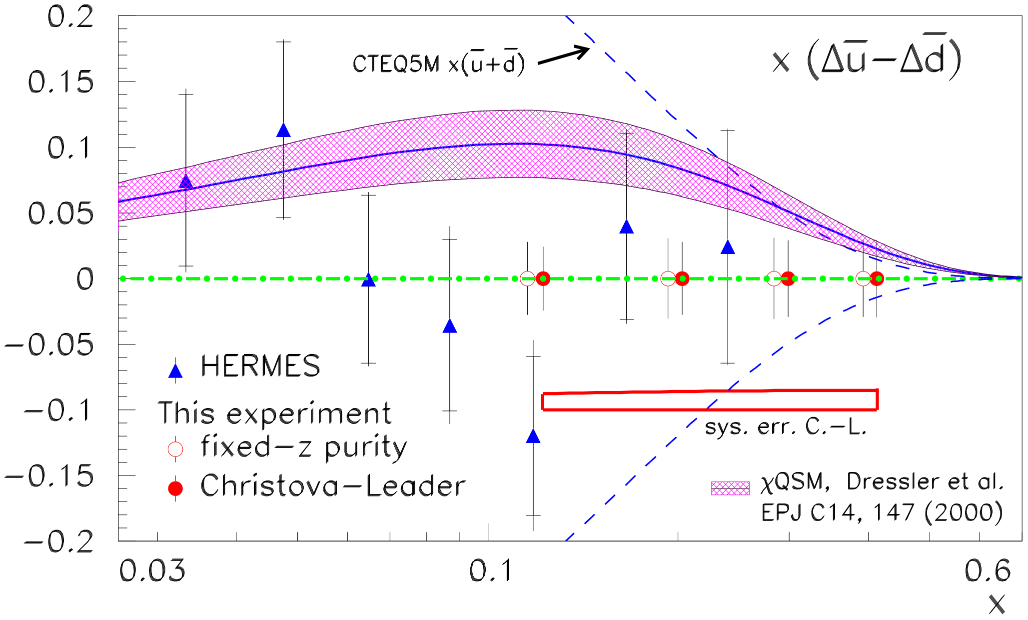

Figure 27: The expected accuracies of $x(\Delta\bar{u} - \Delta\bar{d})$ according to two flavor decomposition methods (fixed-z purity and Christova-Leader) of this experiment are compared with the HERMES data. A chiral soliton model prediction is also plotted together with positivity bounds of $x(\bar{u} + \bar{d})$ from CTEQ5M.

8 Collaboration and responsibility

Members of this collaboration has vast experience running the UVa polarized target at JLab and SLAC. Groups involved in building the calorimeter for the Hall C G_{Ep}/G_{Mp} are participating in this experiment. We expect the JLab target group in tandem with the UVa polarized target group will handle installation, calibration and operation of the polarized target as was done in previous Hall C experiments using the polarized target. The collaboration has a large overlap with the approved SANE experiments which can be run back-to-back together with this experiment without requesting any switch-over time. Members of this collaboration have experience carrying-out spin structure measurements at SLAC, JLab Hall A and Hall C.

9 Summary

We propose to measure the spin asymmetries in semi-inclusive deep-inelastic $\vec{p}(e, e'h)X$ and $\vec{d}(e, e'h)X$ reactions ($h = \pi^+, \pi^-, K^+$ and K^-) on longitudinally polarized NH_3 and LiD targets. The scattered electron will be detected in the large solid angle $BETA$ detector in the same configuration as in the SANE experiment. The HMS spectrometer will detect the hadrons at 10.8° and particle separation of $K/\pi/e$ can be done with standard HMS detectors. A high statistic measurement of the double-spin asymmetries ($A_{1p}^{\pi^\pm}$, $A_{1p}^{K^\pm}$, $A_{1d}^{\pi^\pm}$, $A_{1d}^{K^\pm}$) will be done in the kinematic region of

$x = 0.12 \sim 0.41$ at $Q^2 = 1.21 \sim 3.14$ GeV^2 with leading hadron at $z = 0.5 \sim 0.7$. The experiment will focus on the measurement of the combined asymmetry, $A_{1N}^{\pi^+-\pi^-}$, in which the ratio of π^- to π^+ cross-sections is needed. When changing from π^- to π^+ reaction the acceptance of the electron in the $BETA$ detector will not change and the acceptance of the HMS is well understood. Based on the measurement of $A_{1N}^{\pi^+-\pi^-}$, a leading-order as well as a next-to-leading order spin-flavor decomposition of Δu_v, Δd_v and $\Delta\bar{u} - \Delta\bar{d}$ will be done. In addition to $A_{1N}^{\pi^+-\pi^-}$ method of flavor decomposition, three other leading order methods and the global next-to-leading order fit method of flavor decomposition will be applied independently to provide consistency cross-checks. The possible flavor asymmetry of the polarized sea will be addressed in this experiment.

Two other important physics questions can also be addressed by this experiment. The target single-spin asymmetry A_{UL} will be measured with high precision. Especially, the term $A_{UL}^{sin2\phi_h}$, which at the leading order is produced only through a non-vanishing T-odd Collins fragmentation function, will be measured. In addition, the combined asymmetry, $A_{1N}^{\pi^++\pi^-}$, will be measured. In the naive leading order factorization assumption, the combined asymmetry, $A_{1N}^{\pi^++\pi^-}$, and the inclusive asymmetry A_{1N} should be identical. Differences between $A_{1N}^{\pi^++\pi^-}$ and A_{1N} indicate the level of breakdown of the leading order factorization assumption. In this way, within the same data set, the experiment has an handle on the size of the breakdown in the factorization assumption which introduces systematic uncertainties in the leading order flavor decomposition.

We believe that this experiment will have a strong impact on our understanding of nucleon spin structure. The success of this experiment will set a baseline and will pave the way for future semi-inclusive measurements at the upgraded JLab. A total of 25 days of beam time is requested at 6 GeV in Hall C.

10 Appendix A: The predicted asymmetries at leading order and the next-to-leading order

The predicted asymmetries [19] of $A_{1N}^{\pi^+}$ and $A_{1N}^{\pi^-}$ at leading order and the next-to-leading order are shown in Fig. 28 for each x bin of this experiment as functions of z. The combined asymmetries of $A_{1N}^{\pi^+ \pm \pi^-}$ are shown in Fig. 29.

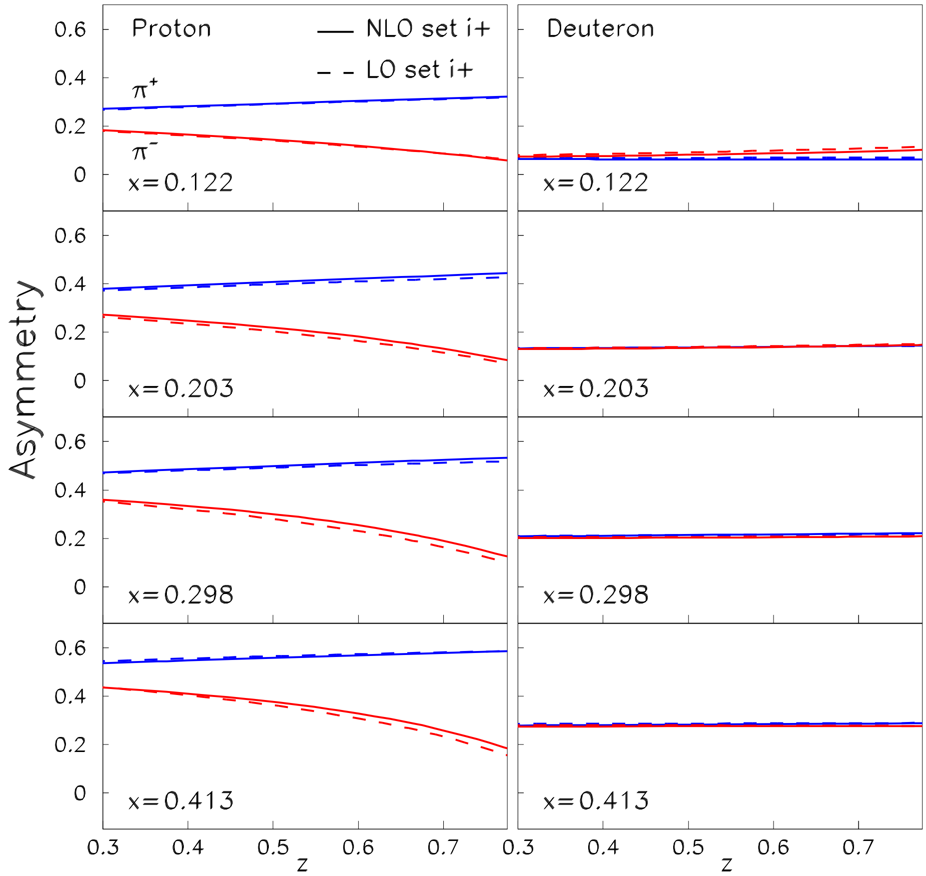

Figure 28: The next-to-leading-order (solid lines) and the leading order (dashed lines) pion asymmetry predictions [19] using de Florian and Sassot's parton distributions [16] set $i+$ are plotted for $\langle Q^2 \rangle = 2.2$ GeV^2 as functions of z.

11 Appendix B: Details of flavor decomposition and tests of leading order factorization

Following the short-hand notation of Ref [8], we take the spin-independent cross section as:

$$\sigma^h(x, z) = \sum_f e_f^2 q_f(x) \cdot D_{q_f}^h(z), \tag{38}$$

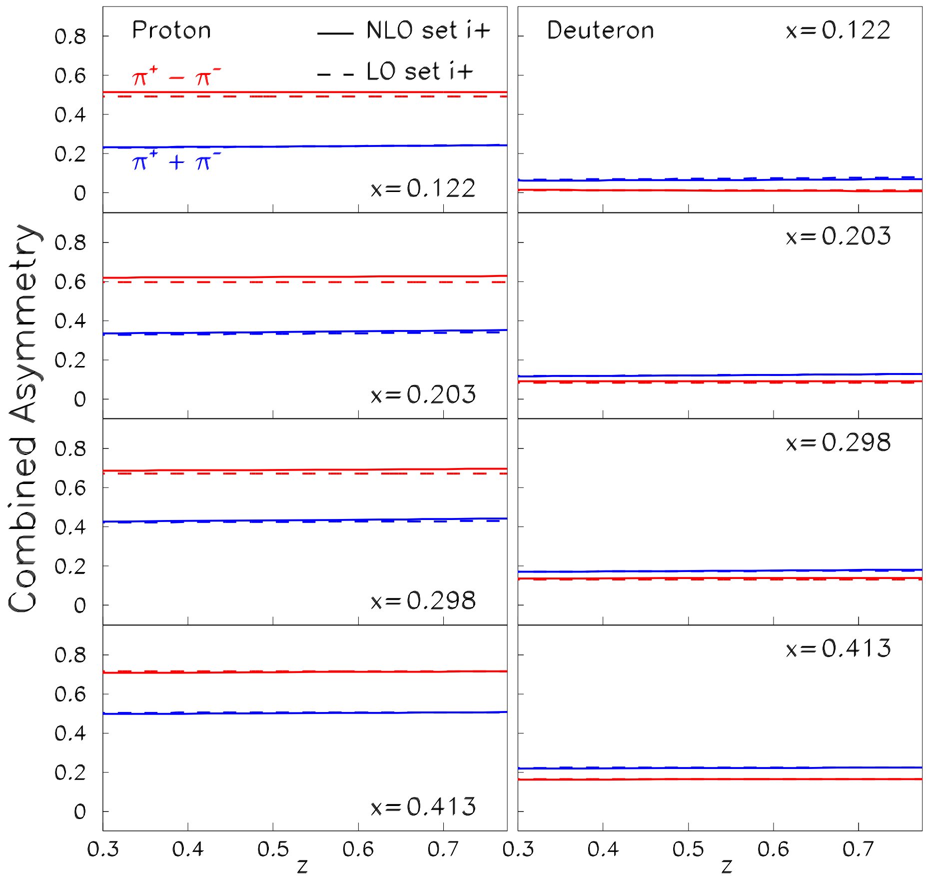

Figure 29: The next-to-leading-order (solid lines) and the leading order (dashed lines) combined pion asymmetry predictions [19] using de Florian and Sassot's parton distributions [16] set $i+$ are plotted for $\langle Q^2 \rangle = 2.2$ GeV^2 as functions of z.

and the spin-dependent cross section as:

$$\Delta\sigma^h(x,z) = \sigma^h_{++} - \sigma^h_{+-} = \sum_f e_f^2 \Delta q_f(x) \cdot D^h_{q_f}(z), \tag{39}$$

where σ^h_{ij} refers to an electron of helicity-i and nucleon of helicity-j. Assuming isospin symmetry and charge conjugation invariance, the number of quark to pion fragmentation functions is reduced to three types: the favored (D^+_π), the unfavored (D^-_π) and the s-quark (D^π_s) fragmentation functions:

$$\begin{aligned}
D^+_\pi &\equiv D^{\pi^+}_u = D^{\pi^-}_d = D^{\pi^-}_{\bar{u}} = D^{\pi^+}_{\bar{d}}, \\
D^-_\pi &\equiv D^{\pi^-}_u = D^{\pi^+}_d = D^{\pi^+}_{\bar{u}} = D^{\pi^-}_{\bar{d}}, \\
D^\pi_s &\equiv D^{\pi^+}_s = D^{\pi^-}_{\bar{s}} = D^{\pi^+}_{\bar{u}} = D^{\pi^+}_{\bar{s}}.
\end{aligned} \tag{40}$$

For the quark to kaon fragmentation functions, the following relations are valid under charge conjugation [28]:

$$\begin{aligned}
D^+_K &\equiv D^{K^+}_u = D^{K^-}_{\bar{u}} = D^{K^+}_{\bar{s}} = D^{K^-}_s, \\
D^-_K &\equiv D^{K^-}_u = D^{K^+}_{\bar{u}} = D^{K^-}_{\bar{s}} = D^{K^+}_s, \\
D^K_d &\equiv D^{K^+}_d = D^{K^+}_{\bar{d}} = D^{K^-}_{\bar{d}} = D^{K^-}_d.
\end{aligned} \tag{41}$$

For this experiment, which covers $0.12 < x < 0.43$, we will assume a symmetrical strange quark distribution and polarization ($s(x) = \bar{s}(x)$, $\Delta s(x) = \Delta\bar{s}(x)$) and neglect heavy quark contributions.

11.1 Spin-dependent and spin-independent cross sections

According to Eq. 38, semi-inclusive π^+ and π^- cross section on proton and neutron are:

$$\begin{aligned}
9\sigma^{\pi^+}_p &= (4u+\bar{d})D^+_\pi + (4\bar{u}+d)D^-_\pi + (s+\bar{s})D^\pi_s, \\
9\sigma^{\pi^-}_p &= (4u+\bar{d})D^-_\pi + (4\bar{u}+d)D^+_\pi + (s+\bar{s})D^\pi_s, \\
9\sigma^{\pi^+}_n &= (4d+\bar{u})D^+_\pi + (4\bar{d}+u)D^-_\pi + (s+\bar{s})D^\pi_s, \\
9\sigma^{\pi^-}_n &= (4d+\bar{u})D^-_\pi + (4\bar{d}+u)D^+_\pi + (s+\bar{s})D^\pi_s,
\end{aligned} \tag{42}$$

the explicit x, z, Q^2 dependence has been left out to save space whenever not causing confusion. The semi-inclusive K^+ and K^- cross sections are:

$$\begin{aligned}
9\sigma^{K^+}_p &= (4u+\bar{s})D^+_K + (4\bar{u}+s)D^-_K + (d+\bar{d})D^K_d, \\
9\sigma^{K^-}_p &= (4u+\bar{s})D^-_K + (4\bar{u}+s)D^+_K + (d+\bar{d})D^K_d, \\
9\sigma^{K^+}_n &= (4d+\bar{s})D^+_K + (4\bar{d}+s)D^-_K + (u+\bar{u})D^K_d, \\
9\sigma^{K^-}_n &= (4d+\bar{s})D^-_K + (4\bar{d}+s)D^+_K + (u+\bar{u})D^K_d.
\end{aligned} \tag{43}$$

Therefore, on the deuteron, the cross sections become:

$$
\begin{aligned}
9\sigma_d^{\pi^+} &= (4(u+d)+\bar{u}+\bar{d})D_\pi^+ + (u+d+4(\bar{u}+\bar{d}))D_\pi^- + 2(s+\bar{s})D_s^\pi, \\
9\sigma_d^{\pi^-} &= (4(u+d)+\bar{u}+\bar{d})D_\pi^- + (u+d+4(\bar{u}+\bar{d}))D_\pi^+ + 2(s+\bar{s})D_s^\pi, \\
9\sigma_d^{K^+} &= (4(u+d)+2\bar{s})D_K^+ + (4(\bar{u}+\bar{d})+2s)D_K^- + (u+\bar{u}+d+\bar{d})D_d^K, \\
9\sigma_d^{K^-} &= (4(u+d)+2\bar{s})D_K^- + (4(\bar{u}+\bar{d})+2s)D_K^+ + (u+\bar{u}+d+\bar{d})D_d^K. \qquad (44)
\end{aligned}
$$

To get the spin-dependent cross sections ($\Delta\sigma^h$), one replaces the quark distribution in Eq. 42, 43 and 44 with the quark polarization distribution.

11.2 The asymmetries expressed in "fixed-z purity"

The "fixed-z purity" is defined as the linear coefficients in front of Δq in the expression of double spin asymmetries, $A_1^h = \Delta\sigma^h/\sigma^h$. At the fixed value of z and x, these coefficients are obtained from the unpolarized parton distribution functions and the fragmentation function ratios. Their expression are listed below:

$$
\begin{aligned}
A_{1p}^{\pi^+}(x,z) &= \frac{4\Delta u + \Delta\bar{d} + (4\Delta\bar{u} + \Delta d)\,\lambda_\pi + 2\Delta s\xi_\pi}{4u + \bar{d} + (4\bar{u}+d)\,\lambda_\pi + 2s\;\xi_\pi}, \qquad (45) \\
A_{1p}^{\pi^-}(x,z) &= \frac{(4\Delta u + \Delta\bar{d})\lambda_\pi + 4\Delta\bar{u} + \Delta d + 2\Delta s\xi_\pi}{(4u+\bar{d})\lambda_\pi + 4\bar{u} + d\; + 2s\xi_\pi}, \\
A_{1d}^{\pi^+}(x,z) &= \frac{4(\Delta u + \Delta d) + \Delta\bar{u} + \Delta\bar{d} + \Big(\Delta u + \Delta d + 4(\Delta\bar{u}+\Delta\bar{d})\Big)\,\lambda_\pi + 4\Delta s\xi_\pi}{4(u+d) + \bar{u} + \bar{d} + \Big(u + d + 4(\bar{u}+\bar{d})\Big)\,\lambda_\pi + 4s\xi_\pi}, \\
A_{1d}^{\pi^-}(x,z) &= \frac{\Big(4(\Delta u + \Delta d) + \Delta\bar{u} + \Delta\bar{d}\Big)\,\lambda_\pi + \Delta u + \Delta d + 4(\Delta\bar{u}+\Delta\bar{d}) + 4\Delta s\xi_\pi}{\Big(4(u+d) + \bar{u} + \bar{d}\Big)\,\lambda_\pi + u + d + 4(\bar{u}+\bar{d}) + 4s\xi_\pi}.
\end{aligned}
$$

$$
\begin{aligned}
A_{1p}^{K^+}(x,z) &= \frac{4\Delta u + \Delta s + (4\Delta\bar{u} + \Delta s)\,\lambda_K + (\Delta d + \Delta\bar{d})\xi_K}{4u + s + (4\bar{u}+s)\,\lambda_K + (d+\bar{d})\xi_K}, \qquad (46) \\
A_{1p}^{K^-}(x,z) &= \frac{(4\Delta u + \Delta s)\,\lambda_K + 4\Delta\bar{u} + \Delta s + (\Delta d + \Delta\bar{d})\xi_K}{(4u+\bar{s})\lambda_K + 4\bar{u} + s + (d+\bar{d})\xi_K}, \\
A_{1d}^{K^+}(x,z) &= \frac{4(\Delta u + \Delta d) + 2\Delta s + \Big(4(\Delta\bar{u}+\Delta\bar{d}) + 2\Delta s\Big)\,\lambda_K + (\Delta u + \Delta\bar{u} + \Delta d + \Delta\bar{d})\xi_K}{4(u+d) + 2\bar{s} + \Big(4(\bar{u}+\bar{d}) + 2s\Big)\,\lambda_K + (u+\bar{u}+d+\bar{d})\xi_K}, \\
A_{1d}^{K^-}(x,z) &= \frac{(4(\Delta u + \Delta d) + 2\Delta s)\,\lambda_K + 4(\Delta\bar{u}+\Delta\bar{d}) + 2\Delta s + (\Delta u + \Delta\bar{u} + \Delta d + \Delta\bar{d})\xi_K}{(4(u+d) + 2\bar{s})\,\lambda_K + 4(\bar{u}+\bar{d}) + 2s + (u+\bar{u}+d+\bar{d})\xi_K}.
\end{aligned}
$$

where the fragmentation function ratios are defined as:

$$
\begin{aligned}
\lambda_\pi(z) &= D_\pi^-(z)/D_\pi^+(z), \qquad & \xi_\pi(z) &= D_s^\pi(z)/D_\pi^+(z), \\
\lambda_K(z) &= D_K^-(z)/D_K^+(z), \qquad & \xi_K(z) &= D_d^K(z)/D_K^+(z). \qquad (47)
\end{aligned}
$$

11.3 The combined spin-dependent yield ratios as factorization tests

From the π^+ and π^- yield, one can construct the combined spin-dependent yield ratios in which the fragmentation functions cancel out:

$$A_{1p}^{\pi^+ + \pi^-} = \frac{\Delta\sigma_p^{\pi^+} + \Delta\sigma_p^{\pi^-}}{\sigma_p^{\pi^+} + \sigma_p^{\pi^-}} = \frac{4(\Delta u + \Delta\bar{u}) + \Delta d + \Delta\bar{d} + 2\Delta s \cdot \dfrac{2D_s^{\pi}}{D_{\pi}^{+} + D_{\pi}^{-}}}{4(u + \bar{u}) + d + \bar{d} + 2s\dfrac{2D_s^{\pi}}{D_{\pi}^{+} + D_{\pi}^{-}}}, \tag{48}$$
$$\approx A_{1p}\left[1 + \left(\frac{2s}{4(u+\bar{u}) + d + \bar{d}} - \frac{2\Delta s}{4(\Delta u + \Delta\bar{u}) + \Delta d + \Delta\bar{d}}\right) \cdot \left(1 - \frac{2D_s^{\pi}}{D_{\pi}^{+} + D_{\pi}^{-}}\right)\right],$$

$$A_{1d}^{\pi^+ + \pi^-} = \frac{\Delta\sigma_d^{\pi^+} + \Delta\sigma_d^{\pi^-}}{\sigma_d^{\pi^+} + \sigma_d^{\pi^-}} = \frac{5(\Delta u + \Delta d + \Delta\bar{u} + \Delta\bar{d}) + 4\Delta s\dfrac{2D_s^{\pi}}{D_{\pi}^{+} + D_{\pi}^{-}}}{5(u + d + \bar{u} + \bar{d}) + 4s\dfrac{2D_s^{\pi}}{D_{\pi}^{+} + D_{\pi}^{-}}}, \tag{49}$$
$$\approx A_{1d}\left[1 + \left(\frac{4s}{5(u+\bar{u}+d+\bar{d})} - \frac{4\Delta s}{5(\Delta u + \Delta\bar{u} + \Delta d + \Delta\bar{d})}\right) \cdot \left(1 - \frac{2D_s^{\pi}}{D_{\pi}^{+} + D_{\pi}^{-}}\right)\right],$$

In Eq. 48 and Eq. 49, the left hand side are taken from semi-inclusive measurements which depend on x, z (and Q^2), but the right-hand side can be determined mostly from the inclusive asymmetries while the left-over z-dependent terms are "double suppressed" by the strange to non-strange quark ratios and the fragmentation function ratio $2D_s^{\pi}/(D_{\pi}^{+} + D_{\pi}^{-})$.

The fragmentation functions and the strange quark effects can also be canceled out in the combined asymmetries involving $\pi^+ - \pi^-$ or $K^+ - K^-$ yields. These type of asymmetries tends to results in larger experimental uncertainties since they involve the difference between two numbers in the dominator. For completeness, these observables are listed below:

$$\begin{aligned} A_{1p}^{\pi^+ - \pi^-} &= \frac{\Delta\sigma_p^{\pi^+} - \Delta\sigma_p^{\pi^-}}{\sigma_p^{\pi^+} - \sigma_p^{\pi^-}} = \frac{4\Delta u_v - \Delta d_v}{4u_v - d_v}, \\ A_{1d}^{\pi^+ - \pi^-} &= \frac{\Delta\sigma_d^{\pi^+} - \Delta\sigma_d^{\pi^-}}{\sigma_d^{\pi^+} - \sigma_d^{\pi^-}} = \frac{\Delta u_v + \Delta d_v}{u_v + d_v}. \end{aligned} \tag{50}$$

There are other "clean observables", for example:

$$\begin{aligned} A_{1p}^{K^+ - K^-} &= \frac{\Delta\sigma_p^{K^+} - \Delta\sigma_p^{K^-}}{\sigma_p^{K^+} - \sigma_p^{K^-}} = \frac{\Delta u_v}{u_v}, \\ A_{1d}^{K^+ - K^-} &= \frac{\Delta\sigma_d^{K^+} - \Delta\sigma_d^{K^-}}{\sigma_d^{K^+} - \sigma_d^{K^-}} = \frac{\Delta u_v + \Delta d_v}{u_v + d_v}. \end{aligned} \tag{51}$$

12 Appendix C: A plan of parasitic data taking during the SANE experiment

How does the semi-inclusive asymmetry change if the missing mass is at the resonance region (and high z) ? Will $A_{1p}^{\pi^+}(x,z)$ still be close to the inclusive asymmetry A_{1p} due to the possible parton-hadron duality in the spin observables ?

The Spin Asymmetries on the Nucleon Experiment (SANE) will measure spin asymmetries in inclusive electron scattering at a beam energies of 4.8 and 6 GeV and scattered electron angle of 40°. As described in the instrumentation section, SANE will use *BETA* to detect the scattered electrons. SANE plans to measure inclusive spin asymmetries on NH_3 polarized target with the target field parallel and at 80° to the beam direction. When the target field is parallel to the beam direction, the wide +-50° conical shaped aperture of the target magnet coils is pointing along beam direction which means that there is a clear path to the HMS inside of 50°. The SANE proposal states that the HMS would be free for parasitic measurements for about half of the requested beam time. The SANE experiment plans to run in the parallel target field configuration at a beam energy of 4.8 and 6.0 GeV for 70 and 100 hours, respectively.

We propose as a parasitic add-on to the SANE experiment to measure coincidence spin asymmetries for the reaction $\vec{p}(\vec{e},e'\pi^+)$ during running of SANE with the parallel target field and the polarized NH_3 target. At a beam energy of 6.0 GeV, the pions would be detected in the HMS at 13.1° and a central momentum of 4.0 GeV. The nominal kinematics of the parasitic data taking is listed in Table. 10. The kinematic coverage for the various kinematic variables is plotted in Fig. 30. The standard HMS gas Cerenkov would be operated at 1.3 atm, so the pions with momentum above 3 GeV/c would fire the Cerenkov and can be separated from kaons and protons. The pions would be separated from positrons using the HMS calorimeter.

The rates of the $\vec{p}(\vec{e},e'\pi^+)X$ reaction on the polarized NH_3 target for each of the four x bins are given in Table 11 assuming 100 nA beam current. The total number of events, N , and the expected errors on the count asymmetry, $\delta A_{\parallel}^{\pi^+}$, for each x bin are listed in Table 11 for 50 hours of coincidence running. Assuming the polarization of the target, P_T, is 80% and a beam polarization of 80% with a dilution factor, f_π, of 0.17. The kinematic factor, $\mathcal{P}_{kin}$, is defined in Eq. 9 in Section 2.2 and is close to one for all x bins. The expected errors on the spin asymmetry, $\delta A_{1p}^{\pi^+}$, for each x-bin is listed in Table 11.

E' GeV	θ_e deg.	$\langle x \rangle$	W GeV	Q^2 GeV^2	z	W' GeV
0.75	40	0.15	3.04	1.50	0.76	1.59
0.90	40	0.23	2.88	2.17	0.78	1.40
1.02	40	0.31	2.70	2.92	0.80	1.32
1.14	40	0.40	2.51	3.58	0.81	1.25

Table 10: The nominal kinematics for the parasitic measurement during the SANE experiment at a central calorimeter angle of 40° and the HMS angle of 13.1° and HMS momentum setting p_{HMS} = 4.0 GeV/c. The corresponding z-coverage, W' values are listed. Data of all x-bins will be collected simultaneously.

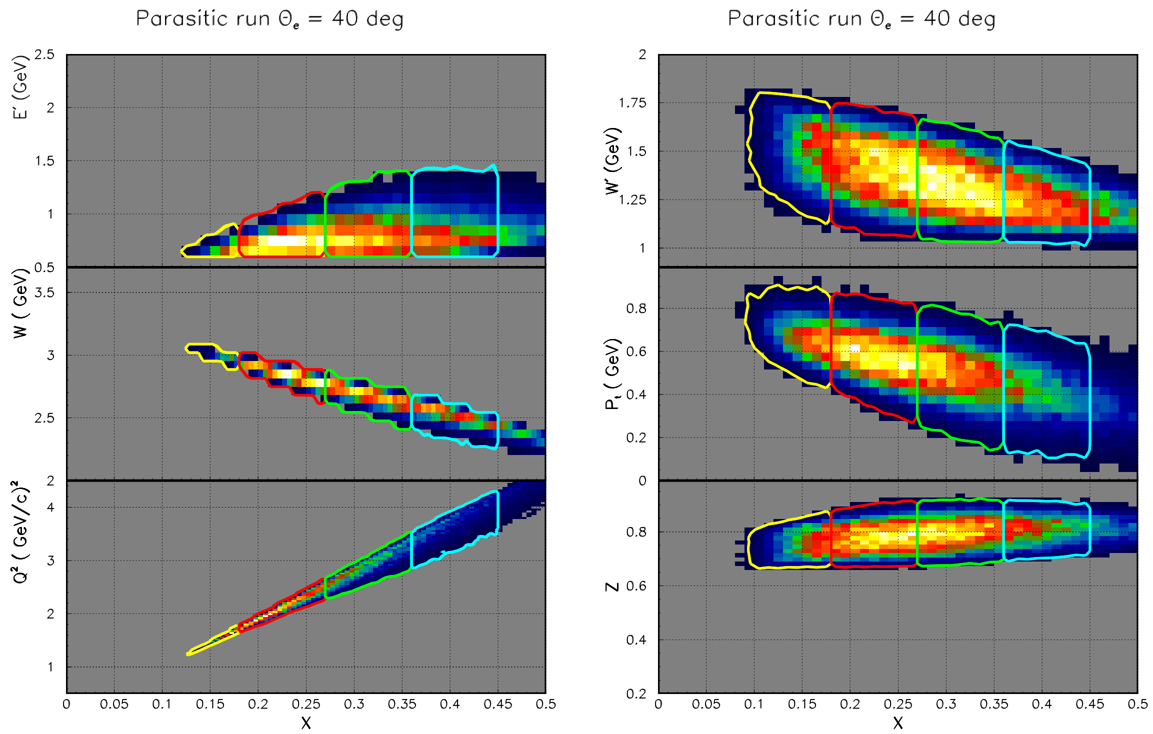

Figure 30: Histograms of various kinematics quantities versus x for the the parasitic measurement during SANE at a central calorimeter angle of 40°.

Pion rates and the total number of events on the NH_3 target:

$\langle x \rangle$	R^{π^+} Hz	N^{π^+} k	$f^\pi P_B P_T \mathcal{P}_{kin}$	$\delta A_{\parallel}^{\pi^+}$ %	$\delta A_{1p}^{\pi^+}$ %
0.15	0.014	2.5	0.19	2.0	10.5
0.23	0.062	11.2	0.18	0.95	5.3
0.31	0.044	7.9	0.17	1.1	6.6
0.40	0.010	1.8	0.16	2.3	14.4

Table 11: Expected rates and statistical uncertainties of the parasitic data taking on the NH_3 target.

References

1. L. L. Frankfurt, M. I. Strikman, L. Mankiewicz, A. Schafer, E. Rondio, A. Sandacz and V. Papavassiliou, Phys. Lett. B **230**, 141 (1989); F. E. Close and R. G. Milner, Phys. Rev. D **44**, 3691 (1991).
2. The HERMES collaboration, *Phys. Rev. Lett.* **92**, 012005 (2004).
3. J. Wendland, Ph.D. Dissertation, Simon Fraser University, September (2003), and earlier analysis results in: M.C. Simani, Ph.D. Dissertation, Vrije University (2002), M. Beckmann, Ph.D. Dissertation, Albert-Ludwigs-University Freiburg, May (2000),
4. The Spin Muon Collaboration, *Phys. Lett.* B **420**, 180 (1998).
5. H. Avakian, for the CLAS Collaboration, the proceeding of the "X-th Workshop on High Energy Spin Physics",September 16-20, 2003.
6. Xiangdong Ji, Jian-Ping Ma and Feng Yuan, hep-ph/0404183.
7. Xiangdong Ji, Jian-Ping Ma and Feng Yuan, hep-ph/0405085.
8. E. Christova and E. Leader *Phys. Lett.* B **468**, 299 (1999) and *Nucl. Phys.* B **607**, 369 (2001).
9. Jefferson Lab E99117, spokespersons Z.-E. Meziani, J.P. Chen, P. Souder. X. Zheng, *et al.*, *Phys. Rev. Lett.* **92**, 012004 (2004), and nucl-ex/0405006.
10. A. N. Sissakian, O. Yu. Shevchenko and O. N. Ivanov, *Phys. Rev.* D **68**, 031502 (2003).
11. A. N. Sissakian, O. Yu. Shevchenko and O. N. Ivanov, hep-ph/0312084.
12. P. Amaudruz *et al.*, *Phys. Rev. Lett.* **66**, 2712 (1991); M. Arneodo *et al.*, *Phys. Rev.* D **55**, R1 (1994).
13. F. M. Steffens, *Phys. Lett.* B **541**, 346 (2002).
14. D. Graudenz, *Nucl. Phys.* B **432**, 351 (1994).
15. D. de Florian, C. A. Garcia Canal, R. Sassot, *Nucl. Phys.* B **470**, 195 (1996).
16. D. de Florian and R. Sassot, *Phys. Rev.* D **62**, 094025 (2000), and D. de Florian, O. A. Sampayo and R. Sassot, *Phys. Rev.* D **57**, 5803 (1998)
17. Marco Stratmann and Werner Vogelsang, *Phys. Rev.* D **64**, 114007 (2001)
18. O.A. Rondon, *Phys. Rev.* C **60**, 035201 (1999).
19. G. Navarro and R. Sassot, private communications 2004.

20. J.M. Niczyporuk and E.E.W. Bruins, *Phys. Rev.* D **58**, 091501 (1998).
21. B. Anderson, G. Gustafson, G. Ingelmann, and T. Sjöstrand, *Phys. Rep.* **97**, 31 (1983).
22. Glück, M. *et al.*, *Phys. Rev.* D **63**, 094005 (2001).
23. Blümlein, J., Böttcher, H., hep–ph/0203155, *Nucl. Phys. B*, (2002) in press.
24. Dressler, B. *et al.*, *Eur. Phys. J.* **C14**, 147 (2000).
25. Bourrely, C. *et al.*, *Eur. Phys. J.* **C23**, 487 (2002).
26. J. Binnewies, B. A. Kniehl and G. Kramer, *Phys. Rev.* D **52**, 4947 (1995).
27. P. Geiger, Ph.D. Dissertation, Ruprecht-Karls-University, Heidelberg (1998).
28. R. D. Field and R. P. Feynman, *Nucl. Phys.* B **136**, 1 (1978). R. P. Feynman, *Photon-Hadron Interaction*, (Benjamin New York, 1972). *Eur. Phys. J.* **C5**, 461 (1998).
29. E. A. Hawker, *et al.*, *Phys. Rev. Lett.* **80**, 3715 (1998).
30. J. C. Peng, *et al.*, *Phys. Rev.* D **58**, 092004 (1998).
31. J.-C. Peng, *Eur. Phys. J.* A **18**, 395 (2003).
32. E. Eichten, I. Hinchliffe, C. Quigg, *Phys. Rev.* D **45**, 2269 (1992).
33. A. W. Thomas, *Phys. Lett.* B **126**, 97 (1983).
34. R. J. Fries, A. Schafer, *Phys. Lett.* B **443**, 40 (1998).
35. K. G. Boreskov, A. B. Kaidalov, *Eur. Phys. J.* C **10**, 143 (1999).
36. F. G. Cao, A. I. Signal, *Eur. Phys. J.* C **21**, 105 (2001).
37. S. Kumano, M. Miyama, *Phys. Rev.* D **65**, 034012 (2002).
38. R. J. Fries, A. Schafer, C. Weiss, hep-ph/0204060.
39. M. Gluck *et al.*, *Phys. Rev.* D **63**, 094005 (2001).
40. B. Dressler *et al.*, hep-ph/9809487.
41. M. Wakamatsu, T. Watabe, *Phys. Rev.* D **62**, 017506 (2000).
42. A. Dorokhov, hep-ph/0112332.
43. C. Bourrely, J. Soffer, F. Buccella, *Eur. Phys. J.* C **23**, 487 (2002).
44. R. S. Bhalerao, *Phys. Rev.* C **63**, 025208 (2001).
45. A. Efremov, *et al.*, *Nucl. Phys.* A **711**, 84 (2002), and A. Efremov, *et al.*, *Phys. Rev.* D **67**, 114014 (2003).
46. Frank E. Close and Nathan Isgur, *Phys. Lett.* B **509**, 81 (2001)
47. C. J. Bebek, *et al.*, *Phys. Rev. Lett.* **30**, 624 (1973).
48. G. Drews, *et al.*, *Phys. Rev. Lett.* **41**, 1433 (1978).
49. P. J. Mulders, hep-ph/0010199, "Current fragmentation in semi-inclusive leptoproduction".
50. T. Sloan, G. Smadja and R. Voss, *Phys Rep.* 162 (1988) 45.
51. JLab-PAC24 proposal E03-109, "Spin Asymmetries on the Nucleon Experiment" (SANE), S. Choi, Z.-E. Meziani and O.A. Rondon co-spokespersons.
52. N.W. Schellingerhout *et al.* Phys. Rev. C 48, 2714 (1993)
53. E155 Collaboration: P Anthony *et al.* Phys. Lett. B 463 (1999) 339.
54. S. Bültmann *et al.*, Nucl. Instr. Meth., A425 (1999) 23.
55. Lai, H.L. *et al.*, *Eur. Phys. J.* **C12**, 375 (2000).
56. S. Kretzer, E. Leader and E. Christova, *Eur. Phys. J.* C **22**, 269 (2001).

57. HERMES Collaboration preliminary results (http://www-hermes.desy.de).
58. J. Blumlein and H. Bottcher, hep-ph/0203155.
59. D. Gaskell, private communication.